

FORMATION OF COMPACT CLUSTERS FROM HIGH RESOLUTION HYBRID COSMOLOGICAL SIMULATIONS

MARK L. A. RICHARDSON¹, EVAN SCANNAPIECO¹, AND WILLIAM J. GRAY²

Draft version June 27, 2022

ABSTRACT

The early Universe hosted a large population of small dark matter ‘minihalos’ that were too small to cool and form stars on their own. These existed as static objects around larger galaxies until acted upon by some outside influence. Outflows, which have been observed around a variety of galaxies, can provide this influence in such a way as to collapse, rather than disperse the minihalo gas. Gray & Scannapieco performed an investigation in which idealized spherically-symmetric minihalos were struck by enriched outflows. Here we perform high-resolution cosmological simulations that form realistic minihalos, which we then extract to perform a large suite of simulations of outflow-minihalo interactions including non-equilibrium chemical reactions. In all models, the shocked minihalo forms molecules through non-equilibrium reactions, and then cools to form dense chemically homogenous clumps of star-forming gas. The formation of these high-redshift clusters will be observable with the next generation of telescopes, and the largest of them should survive to the present day, having properties similar to halo globular clusters.

1. INTRODUCTION

The observed history of large-scale structure formation is well explained by the cold dark matter model with a cosmological constant term (e.g., Spergel et al. 2007; Larson et al. 2011). This theory posits that small-scale perturbations in the dark matter density merged hierarchically over time, leading to larger perturbations that continued to coalesce into even larger structures, while underdensities became large voids (e.g., White & Rees 1978; White & Frenk 1991; Kauffmann et al. 1993; Cole et al. 2000; Bower et al. 2006). The gas dynamics were almost completely dictated by these dark matter potentials. Thus, massive baryonic objects formed at later times, while a large population of smaller objects formed early.

At the poorly constrained redshifts before reionization, it is then expected that there existed a large population of small gravitationally bound clumps of dark matter and gas, whose masses were much smaller than galaxies today. At temperatures below $\approx 10^4$ K, transitions in atomic hydrogen and helium are not excited, leaving gas to cool radiatively through molecular excitations and dust emission. Although some molecules may have survived from recombination and cooled the earliest structures (e.g., Abel et al. 2002; Bromm & Clarke 2002; Turk et al. 2009; Stacy et al. 2010), they would have produced stars that disassociated these molecules, suppressing cooling in neighboring perturbations (Galli & Palla 1998). Furthermore, it is unlikely that even with some molecules surviving further, they could have effectively cooled such small structures (e.g. Whalen et al. 2008; Ahn et al. 2009). Thus, the subset of these low-mass objects with virial temperatures below 10^4 K, so-called “minihalos”, persisted as sterile objects, unable to cool and form stars without an external influence.

Some of these minihalos may have been located near starbursting galaxies, which can drive outflows powered by supernovae, as have been observed around a variety of galaxies at a range of redshifts (e.g., Lehnert & Heckman 1996; Franx et al. 1997; Pettini et al. 1998; Martin 1999; Heckman et al. 2000; Veilleux et al. 2005; Rupke et al. 2005; Chung et al. 2011). It is expected that these observed starbursts are a small example of a much larger, earlier population that predated, and likely drove, reionization (Scannapieco et al. 2002; Thacker et al. 2002; Ferrara & Loeb 2013). Although these galaxies also produced ionization fronts that disassociated their environments, Fujita et al. (2003) showed that the outflows of such galaxies can trap this ionizing radiation, shadowing regions around the starbursting galaxies. Thus, some neutral minihalos could have been sheltered from ionization fronts, and interacted with a kinematic outflow first. Furthermore such interactions, through non-equilibrium processes, could have induced the formation of molecular gas that could cool the gas sufficiently to induce star-formation.

Gray & Scannapieco (2010; 2011A; 2011B) (hereafter GS10, GS11A, GS11B) performed idealized simulations of this interaction, which featured a spherical isothermal gas cloud embedded in a static analytic dark matter potential. Together the dark matter and gas represented a minihalo, which followed an NFW radial density profile (Navarro et al. 1997), and it was embedded in a uniform background. The starburst outflow, on the other hand, was modeled as a plane-parallel shock of material inflowing from the x boundary. GS10 also enacted a 14-species primordial non-equilibrium chemical network with associated cooling terms. As the shock struck the minihalo, it catalyzed the creation of H_2 , while mixing in some of its enriched material. As much as 100% of the baryonic material of the minihalo collapsed into a small ribbon of gas that extended well out of the dark matter potential, that then cooled via H_2 . They found that the ribbon eventually collapsed into several distinct clumps, whose properties were remarkably similar to present-day halo globular

¹ School of Earth and Space Exploration, Arizona State University, Tempe, AZ 85287

² Lawrence Livermore National Laboratory, P.O. Box 808, L-038, Livermore, CA 94550, USA

clusters. GS11A enacted a K - L two-equation sub-grid turbulence module and metal-line cooling, which allowed for more efficient mixing of enriched shock material into the collapsed minihalo gas, and allowed this enriched material to add to the net cooling. GS11A found very similar results as GS10, producing a population of clusters very much like halo globular clusters. Finally, GS11B performed a parameter suite that looked into the effect of minihalo mass, clumping factor, and angular momentum, outflow energy and enrichment, minihalo-starburst separation, redshift, and UV background on the characteristics of the interaction and its resulting clusters.

Cosmological simulations show that virialized structures are typically found at the nodes of a fractal-like cosmic web (e.g. Springel et al. 2005A). Thus minihalos were found at the intersections of cosmic filaments, likely with higher-mass objects nearby. Their dark matter was a dynamic background, that responded to gas dynamics. Although the average radial profile of minihalos likely did follow an NFW profile, they were not perfectly isotropic. These characteristics make minihalos quite different than the idealized gas clouds simulated in GS10, GS11A, and GS11B.

In fact, the isotropy in their work may have been the cause of the small collapsed ribbon of material along the x -axis, resulting from the shock wave converging at the antipodal point. It is also unclear how reasonable it is to treat the dark matter as a static analytic term. As densities in the collapsing gas eventually exceeded those in the dark matter, perhaps a more dynamic treatment of the dark matter might uncover motions that significantly affect the future evolution of the gas.

In this work, we address these issues by generating a range of minihalos in high-resolution cosmological simulations. Then, having isolated the desired objects and their immediate environments into a new simulation volume, we simulate their interactions with starburst-driven outflows. In this way we are able to understand this interaction in much more detail as it occurred in the early Universe, and contrast it with the idealized minihalo-outflow simulations previously undertaken.

The structure of this paper is as follows. In §2 we describe the cosmological simulations, and the outflow-minihalo interaction simulations, followed by our post-processing techniques. In §3 we discuss the results from our parameter suite, and in §4 we present simulated high and low-redshift observables derived from these results. We summarize our work and give conclusions in §5. Throughout this paper we use $(\Omega_\Lambda, \Omega_M, \Omega_b, n, \sigma_8, h_{100}^{-1}) = (0.734, 0.266, 0.0449, 0.963, 0.801, 0.71)$ (Larson et al. 2011).

2. NUMERICAL METHODS

2.1. Particle Simulations

As a first step, we performed a low-resolution cosmological simulation using the smoothed-particle hydrodynamic code GADGET-2 (Springel et al. 2001; Springel 2005B) in a box that was 2.57 comoving Mpc on a side. This had 2 spherically nested resolution levels, the lowest resolution level spanning the whole volume, and the next level spanning a sphere centered in the box with a radius a quarter of the box size. Each level had effectively 192^3 dark matter particles (with masses of $7.39 \times 10^4 M_\odot$ and

$9.24 \times 10^3 M_\odot$) and 192^3 gas particles (with masses of $1.51 \times 10^4 M_\odot$ and $1.87 \times 10^3 M_\odot$). At each level of resolution the modes of the initial spectrum are truncated to ensure there is no aliasing of high k modes into the low k values (as in Thacker & Couchman 2000; Richardson et al. 2013). Initial conditions were generated using the transfer function from CAMB (Lewis et al. 2000), assuming an initial spectral slope of $n = 0.963$. CAMB uses a line-of-sight implementation of the linearized equations of the covariant approach to cosmic microwave background (CMB) anisotropies. This results in different transfer functions for the dark matter and baryon components, with the two weighted together to yield the total transfer function. This simulation began at $z = 199$ and was evolved to $z = 15.4$. We did not include star formation or feedback, but did include atomic and molecular cooling. We calculated the different ionization states of hydrogen and helium from the density and temperature following Katz et al. (1996). Although at such a high-redshift collisional ionization equilibrium is perhaps not appropriate, this assumption is irrelevant since the material remains neutral. We assumed a primordial number density fraction of molecular hydrogen of $H_2/H = 1.1 \times 10^{-6}$ following Palla & Galli (2000) and a primordial deuterium number density fraction of $D/H = 2.7 \times 10^{-5}$ following Steigman (2009). Using the baryon-to-light ratio of $\eta = 6.0 \times 10^{-10}$ from Steigman (2009), we set the deuterated hydrogen number density fraction at $HD/H_2 = 6 \times 10^{-4}$ from Palla & Galli (2000). Given these abundances, we employed the molecular cooling rates of GS10 and cooling rates for Compton scattering against CMB photons as given in Barkana & Loeb (2001).

We then used the friends-of-friends algorithm (Davis et al. 1985) to determine groups that corresponded to an overdensity of 180 with a linking length of 1.19 kpc, expected to be virialized from a spherical top-hat collapse model. We focused on three groups, with total masses of $2.0 \times 10^6 M_\odot$, $4.0 \times 10^6 M_\odot$, and $8.0 \times 10^6 M_\odot$, respectively. For each group, we performed a simulation statistically identical to the low-resolution simulation, but with additional resolution centered on the group. We added two additional spherically-nested resolution levels resulting in particle masses of $144 M_\odot$ and $29.3 M_\odot$ for dark matter and baryons, respectively, at the highest resolution.

These high-resolution initial conditions were evolved to $z = 14$. We then located groups using the HOP group finder (Eisenstein & Hut 1998) implemented in the yt visualization and analysis toolkit (Turk et al. 2011) with masses, in units of $10^6 M_\odot$, of $M_6 = 0.716, 1.38, 2.33, 2.72, 7.17$, and 18.7 . For each suitable halo, we isolated regions out to 5 virial radii, r_v , of the group in the GADGET-2 snapshots and mapped these to the adaptive mesh refinement code FLASH3.2 (Fryxell et al. 2000) using the procedure discussed in Richardson et al. (2013). A summary of the simulations is given in Table 1. For the $z \leq 14$ simulations, we extended the $z = 14$ datasets by scaling position, velocity and energy by the scale factor difference. The majority of these simulations were done at $z = 8$ as it is the most likely to be directly observable.

2.2. AMR Simulations

TABLE 1
SIMULATIONS SUMMARY

SPH Parameters:	SPH z_{init}	SPH z_f	SPH m_{DM}	SPH m_{gas}	Box size					
	199	14	144 M_{\odot}	29.3 M_{\odot}	2.57 Mpc					
AMR Simulation	M_6	r_{vir} (pc)	Δx (pc)	Outflow path	v_s (km s $^{-1}$)	μ_s	E_{55}	σ_5	z	$Z(Z_{\odot})$
FID	2.72	505	5.92	Filament	226	60.4	10.0	2.62	8	0.12
LR	2.72	505	11.8	Filament	226	60.4	10.0	2.62	8	0.12
HR	2.72	505	2.96	Filament	226	60.4	10.0	2.62	8	0.12
PO1	2.72	505	5.92	IGM	226	60.4	10.0	2.62	8	0.12
PM07	0.716	320.	3.75	Filament	226	60.4	10.0	2.62	8	0.12
PM1	1.38	402	4.71	Filament	226	60.4	10.0	2.62	8	0.12
PM2	2.33	470.	5.51	Filament	226	60.4	10.0	2.62	8	0.12
PM7	7.17	693	8.12	Filament	226	60.4	10.0	2.62	8	0.12
PM19	18.7	967	11.3	Filament	226	60.4	10.0	2.62	8	0.12
Pv75	2.72	505	5.92	Filament	75.0	60.4	30.2	7.91	8	0.12
Pv125	2.72	505	5.92	Filament	125	60.4	18.1	4.74	8	0.12
Pv340	2.72	505	5.92	Filament	340.	60.4	6.66	1.74	8	0.12
Pv510	2.72	505	5.92	Filament	510.	60.4	4.44	1.16	8	0.12
P μ 3	2.72	505	5.92	Filament	226	32.5	1.54	1.14	8	0.12
P μ 8	2.72	505	5.92	Filament	226	77.5	4.59	3.35	8	0.12
P μ 9	2.72	505	5.92	Filament	226	90.0	5.33	3.89	8	0.12
Pz10	2.72	413	4.84	Filament	226	90.7	10.0	3.92	10	0.12
Pz14	2.72	303	3.55	Filament	226	169	10.0	7.30	14	0.12
PZ005	2.72	505	5.92	Filament	226	60.4	10.0	2.62	8	0.005
PZ05	2.72	505	5.92	Filament	226	60.4	10.0	2.62	8	0.05
PZ5	2.72	505	5.92	Filament	226	60.4	10.0	2.62	8	0.5

Notes. M_6 is the minihalo mass in units of $10^6 M_{\odot}$. r_{vir} is the virial radius of the minihalo in units of (physical) pc. Δx is the resolution limit at the highest refinement level in units of (physical) pc. The outflow path describes whether the shock travels along a filament or from the lower density intergalactic medium (IGM). v_s is the shock velocity in units of km s $^{-1}$. μ_s is the shock momentum per unit area, in units of $M_{\odot} \text{pc}^{-1} \text{Myr}^{-1}$. E_{55} is the energy of the shock in units of 10^{55} erg. σ_5 is the surface density of the shock as it enters the box in units of (physical) $10^5 M_{\odot} \text{kpc}^{-2}$. z is the redshift of the interaction. In the event that $z \neq 14$ we translate it to the lower redshift by expanding the $z = 14$ minihalo and cooling it. Z is the metallicity of the incoming shock in solar units.

2.2.1. FLASH and the Dark Matter Gravitational Potential

The mapped GADGET-2 snapshots were treated as initial conditions for simulations performed with FLASH version 3.2, a publicly-available multidimensional adaptive mesh refinement hydrodynamic code (Fryxell et al. 2000) that solves the Riemann problem on a Cartesian grid using a directionally-split piecewise parabolic method (PPM) (Colella & Woodward 1984; Colella & Glaz 1985; Fryxell et al. 1989). FLASH also includes particles that we used to represent dark matter, which we simply moved directly from GADGET to FLASH. Dark matter mass is mapped to the grid after each hydro step using the Cloud-In-Cell (CIC) method (e.g., Birdsall & Fuss 1997), where the particles are assumed to exist in a box of the same size as the grid at the current refinement. The mass is distributed equally over this box and thus the percent of mass mapped into a particular cell is the percentage of the box that overlaps that cell.

To accommodate high-resolution regions with very few particles, we sometimes moved dark matter particles to a lower resolution level, mapping them over a larger box. This was necessary to prevent any low-density gas in the high-refinement region from unrealistically collapsing onto a single dark matter particle. To determine which particles needed this ‘derefine’, a particle count was monitored for each cell. If a cell had three or more neighboring cells that did not contain particles, or if it had two neighboring cells without particles in the same direction, then the particles in that cell were flagged for derefinition, and the same criteria was checked for the parent cell. This criteria was slightly relaxed for particles in cells adjacent to block boundaries, which were always tagged for derefinition if the neighboring block was at a lower refinement level. This was necessary to be consistent

with the criteria used by the cells on the lower resolution block to determine if its neighbors had particles, and it is illustrative of the fact that at a lower refinement level a larger fraction of the box associated with the particles would overlap the neighboring cell.

In all cases, once particles were derefined and mapped to that grid level using the standard CIC method, this material must then be ‘prolonged’ back onto the high-resolution level, from parent to (higher-resolution) child, and added to any density that was directly mapped to that child. The prolongation of the dark matter density into a child cell that was not near the boundary of the block, such that it could see both its parent cell and its parent’s neighbors, was determined by using linear interpolation between this cell’s parent density and its closest neighbor’s density. A quadratic interpolation scheme could have been used, but in rare circumstances this could lead to negative dark matter mapped in some cells. Figure 1 shows a plot of the grid layout of a child and parent block with one dimension. If we assume the density is linearly continuous between parents P1 and P2, then:

$$\begin{aligned}
 \rho_{C2}^{\text{final}} &\equiv \rho_{C2}^{\text{map}} + \rho_{C2}^{\text{prolong}} & (1) \\
 &\equiv \rho_{C2}^{\text{map}} + \Omega_{12}\rho_{P1} + \Omega_{22}\rho_{P2} \\
 &= \rho_{C2}^{\text{map}} + \frac{3}{4}\rho_{P1} + \frac{1}{4}\rho_{P2},
 \end{aligned}$$

where Ω_{ij} is the weighting from parent i into child j , ρ_{C2}^{map} is the dark matter density mapped into child C2 without requiring derefinition, $\rho_{C2}^{\text{prolong}}$ is the amount of dark matter density prolonged into child C2 from derefined particles, and ρ_{C2}^{final} is the sum of the mapped and prolonged dark matter density, which is used for the gravity

calculation. At the borders of blocks, where the child cell

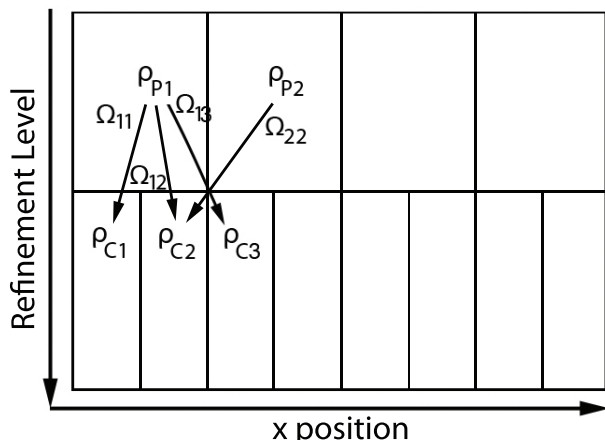


FIG. 1.— Illustration of our gravity procedure in one dimension. A fraction Ω_{ij} of the density from parent P1, ρ_{P1} , is prolonged to child CJ and added to its existing density values, which were mapped from less derefined particles.

could not see one of its parent’s neighbors, we then used a direct mapping from the parents value,

$$\begin{aligned} \rho_{C1}^{\text{final}} &\equiv \rho_{C1}^{\text{map}} + \rho_{C1}^{\text{prolong}} \\ &\equiv \rho_{C1}^{\text{map}} + \Omega_{11}\rho_{P1} \\ &= \rho_{C1}^{\text{map}} + \rho_{P1}. \end{aligned} \quad (2)$$

This limited the demand of inter-processor communication, and resulted in a slight error in the dark matter field on the borders of blocks where dark matter was derefined (see Figure 2). However, this error was much smaller than the error from leaving the dark matter mass at the highest refinement level, and the method still allowed for a much more efficient runtime. Ideally we would like to have filled the guard cells of parent P1 and passed that information to child C1, requiring one interprocessor communication, but in the event that the neighbor of parent P1 was itself a child block, then we would have been unable to pass the acceleration of child C1 back to the parent’s neighbor when we calculated the particle accelerations. We thus opted for a less complex weighting on the boundaries.

The benefit of using this new technique for handling the dark matter density field is clearly illustrated in Figure 2, which shows that individual particles were never mapped to isolated peaks in the dark matter density field.

To cancel out the self-gravitational force from prolonged pieces of the same dark matter particle, the accelerations was ‘restricted’ up to the particle’s refinement level using identical weightings as the prolongation (see Equations 1, 2). Thus:

$$\begin{aligned} \mathbf{a}_{P1} &\equiv \frac{1}{2}(\Omega_{11}\mathbf{a}_{C1} + \Omega_{12}\mathbf{a}_{C2} + \Omega_{13}\mathbf{a}_{C3}) \\ &= \frac{1}{2}(\mathbf{a}_{C1} + \frac{3}{4}\mathbf{a}_{C2} + \frac{1}{4}\mathbf{a}_{C3}), \end{aligned} \quad (3)$$

and then the weighting from the Cloud-in-Cell stage was applied to the acceleration from each cell onto the particle at the same grid level at which it was mapped. This resulted in an exact cancelation of the self-gravitational

force, leaving only the gravitational acceleration from the gas and remaining dark matter particles.

We tested the new particle gravity by tracing the evolution of a pressureless spherical region with a density 8 times the background density, the results of which are shown in Figure 3. The radius begins to collapse slowly, then accelerates. Our new results are indistinguishable from both the results of the earlier particle gravity scheme and the analytic solution.

2.2.2. Outflow Simulations

Using FLASH and the selected GADGET groups, we performed a parameter study on outflows interacting with these groups. We mapped the group region into a rectangular box with the group centered at $(0,0,0)$ pc, with $(-1.5r_v \leq x \leq 4.5r_v)$ and $(-1.5r_v \leq y, z \leq 1.5r_v)$. FLASH is an AMR code with blocks of $N_{B,X} \times N_{B,Y} \times N_{B,Z}$ cells divided between processors. Each subsequent level in refinement increases the spatial resolution by a factor of two in each dimension. Our simulations were run with a maximum of 6 levels of refinement (except for the high and low resolution runs), allowing up to 32 blocks in each direction, where the relative difference in resolution between a block and any of its neighbors can be at most a factor of two. For our simulations we used a root grid of $N_{B,X} = 2N_{B,Y} = 2N_{B,Z} = 16$, accommodating the rectangular box size while maintaining uniform resolution in all directions. This gives a maximum resolution of 256 cells per $3r_{\text{vir}}$.

The outflow with positive x -velocity was added to the x -boundary, following the model of GS10. A Sedov-Taylor solution was used to estimate the conditions of the galactic outflow. We decided on appropriate shock velocities, v_s , and shock surface momentum (per unit area), μ_s , and used these to constrain the conditions of the outflow. We let the initial input energy for the shock be given by $E = \epsilon E_{55}(10^{55} \text{ erg})$, where E_{55} is the energy of the SNe driving the winds in units of 10^{55} erg, and the wind efficiency, ϵ , quantifies the coupling between the SNe and the winds, taken to be 0.3. To be consistent with previous work, we assumed that before reaching our box, the shock had swept up an ambient medium of material with an overdensity, δ_{44} , in units of 44 times the background density taken here to be 1, over the (physical) separation distance, R_s , which leads to a surface density, σ_5 , in units of $10^5 M_{\odot}/\text{kpc}^2$. Thus, for a given shock velocity and momentum we have:

$$R_s = \left(\frac{13.4\delta_{44}^{-1}\mu_s \text{ kpc}}{M_{\odot} \text{ pc}^{-1} \text{ Myr}^{-1}} \right) \left(\frac{\text{km s}^{-1}}{v_s} \right) \left(\frac{9}{1+z} \right)^3, \quad (4)$$

$$\sigma_5 = \left(\frac{9.77\mu_s}{M_{\odot} \text{ pc}^{-1} \text{ Myr}^{-1}} \right) \left(\frac{\text{km s}^{-1}}{v_s} \right), \quad (5)$$

and

$$\begin{aligned} E_{55} &= 3.04 \times 10^{-3} \epsilon^{-1} \delta_{44}^{-2} \times \dots \\ &\dots \left(\frac{\mu_s}{M_{\odot} \text{ pc}^{-1} \text{ Myr}^{-1}} \right)^3 \left(\frac{\text{km s}^{-1}}{v_s} \right) \left(\frac{9}{1+z} \right)^6. \end{aligned} \quad (6)$$

The post-shock temperature is $T_s = 1.4 \times 10^5 (v_s/100 \text{ km s}^{-1}) \text{ K}$, the outflow is fully ionized, and it has an abundance given by Z . The fiducial values

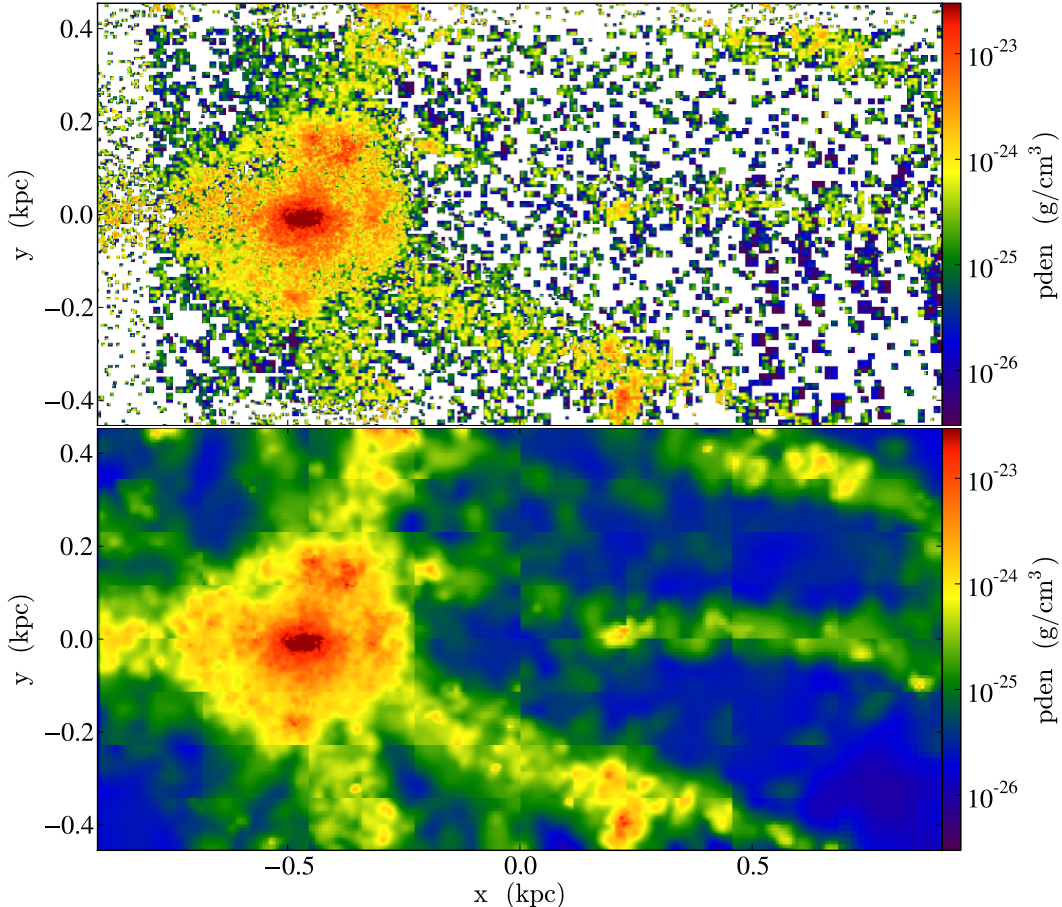


FIG. 2.— Comparison of the density-weighted projection of the dark matter density field, $pden$, of the minihalo in the original non-refined particle gravity routine (top) and with the new derefinement method that smooths the dark matter field (bottom). Regions where there were few dark matter particles moved those particles to lower resolution blocks, increasing the size of their mapped region. Block boundaries are not continuous to limit the number of inter-processor communications. These projections were made using the yt-toolkit (Turk et al. 2011) (<http://yt-project.org/>).

are chosen to match Scannapieco et al. (2004), with $z = 8$, $Z = 0.12 Z_{\odot}$, $v_s = 226 \text{ km s}^{-1}$, $\mu_s = 60.7 M_{\odot} \text{ pc}^{-1} \text{ Myr}^{-1}$, leading to $R_s = 3.6 \text{ kpc}$, $E_{55} = 10$, and $\sigma_5 = 2.62$, and oriented such that the outflow is propagating along an accretion lane, which is the most likely direction pointing towards a neighboring starbursting galaxy. The shock lifetime is estimated from $\sigma_s = \rho_{\text{post}} v_{\text{post}} t_s$, where σ_s is the surface density of the shock, ρ_{post} is the post-shock density, v_{post} is the post-shock velocity, and t_s is the shock lifetime. After 40% of the shock time, the shock was tapered off by slowly lowering the density and raising the temperature, keeping pressure constant to inhibit further refinement. The density falls off exponentially, with

$$\rho(t > 0.4t_s) = \rho_0(0.01 + 0.99e^{-(t-0.4t_s)/(0.6t_s)}), \quad (7)$$

while the temperature increases as $1/\rho(t)$ to maintain a constant post-shock pressure.

We allowed for refinement based on the second derivative of density and pressure. Regions that had their density or pressure profiles vary sufficiently quickly were forced to increase their resolution by a factor of two. After 7 Myr we forced derefinement beyond a cylinder with a radius of $0.8R_v$ aligned with the x -axis for material be-

low $3 \times 10^{-26} \text{ g cm}^{-3}$. This was to prevent low-density mixing from limiting the time-step.

During the AMR simulations, we used the same cooling source terms as in the SPH runs, although we also accounted for possible nonequilibrium chemistry following GS10. This is essential as the interaction between the outflow and the minihalo leads to the creation of coolants such as H_2 and HD.

With this package in place, along with the dark matter gravitational potential calculated as described above, we ran the shock-minihalo simulations until the outflow had collapsed the minihalo material, typically leaving a ribbon of material behind the minihalo. This interaction took between a few million years, and a few tens of million years.

2.2.3. Ballistic Evolution

The timescale of the evolution of this ribbon of material can be up to ten times as long as the timescale of the shock crossing the simulation volume (GS10). To avoid modeling this material for such a long period of time, we simplified its evolution by constructing a series of 64 one-dimensional point-particles, we call “cloud particles”, whose x -positions spanned the space of the

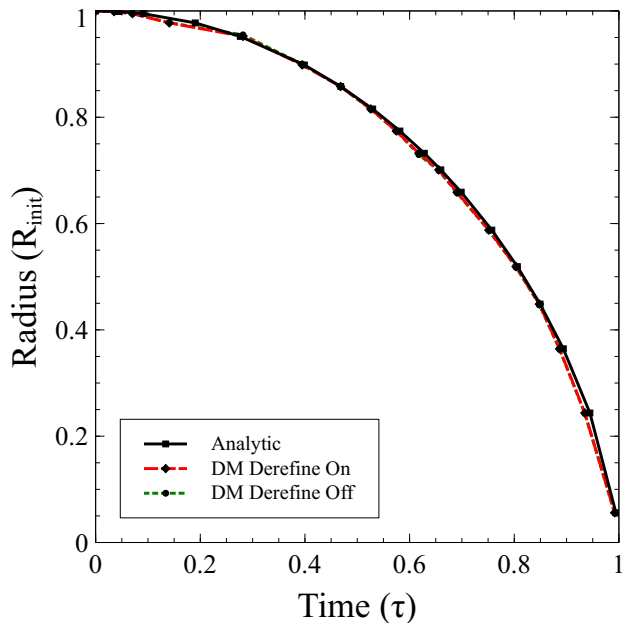


FIG. 3.— Evolution of the radial extent of the overdensity with time. The solid black line with square points shows the analytic solution while the dotted green line with circles shows the simulated result from FLASH without derefining the dark matter, and the red dashed line with diamonds is the result with derefining the dark matter. We see no significant differences between the results of flash regardless of whether the dark matter is derefined or not, and they are consistent with the analytic solution.

ribbon. We then added the mass, momentum and metal abundance of each ribbon segment into a corresponding particle if it was within half the inter-particle spacing in the x -direction from this particle, it was denser than 150% the post-shock density, and its radial velocity away from the x -axis was sufficiently slow as to make it gravitationally bound to this axis on a timescale of 200 Myr.

We determined if a fluid segment was bound by comparing the y - and z -component of the velocity of the fluid with the y - and z -component of the minihalo’s dark matter gravitational potential. Here we assumed a NFW profile (Navarro et al. 1997):

$$\Phi(r) = -\frac{GM_{\text{vir}}}{rF(c)} \log\left(1 + c\frac{r}{r_{\text{vir}}}\right), \quad (8)$$

where G is Newton’s gravitational constant, M_{vir} is the virial radius, assumed to be the same as the minihalo mass, r_{vir} is the virial radius, set by the virial mass and redshift, $F(x) = \log(1+x) - x/(1+x)$, and c is the concentration parameter, assumed to be 4, slightly less than the fiducial value in GS11B since we find the halos in our Gadget simulations are typically less concentrated (e.g., Richardson et al. 2013). For each segment determined to be bound to the x -axis, we added its gravitational potential into radial bins. We then determined the best-fit NFW profile for the radial gravitational potential, fitting for mass and clumping factor, using a Gauss-Newton algorithm. We then rechecked which gas segments were bound to the x -axis using the fitted NFW profile. We iterated this process until the profile fit was self-consistent.

Once we were satisfied with our identification of the bound material, we tracked the variance of the abundance of the particles to determine its uniformity. The

cloud particles were then evolved ballistically for 200 Myr, including their mutual gravitational attraction and the fitted gravitational potential of the minihalo. Finally, when one particle overtook a second one, we merged them into a single new particle, conserving mass and momentum and averaging their abundance while combining their variance.

3. RESULTS

3.1. Fiducial Behavior

Figure 4 shows the evolution of our fiducial run (see FID in Table 1) at 6 characteristic times. This run had a minihalo mass of $M_6 = 2.72$ and a virial radius of 505 pc. Our fiducial outflow had a shock speed of $v_s = 226 \text{ km s}^{-1}$ and surface momentum of $\mu_s = 60.4 M_{\odot} \text{ pc}^{-1} \text{ Myr}^{-1}$, consistent with a starburst-minihalo separation of $R_s = 3.6 \text{ kpc}$, shock surface density of $\sigma_5 = 2.62$ and energy of $E_{55} = 10$. We used a redshift of $z = 8$, and a shock enrichment of $0.12 Z_{\odot}$.

As the shock enters the volume from the left boundary, it travels freely through the diffuse medium, but stalls slightly within the inner 100 pc as it moves along the denser filament. At 2.3 Myr, the shock makes contact with the dense minihalo, and molecular hydrogen begins to form in the swept-up accretion lane. By 6.7 Myr, the shock has overtaken the minihalo in the diffuse medium, and has propagated roughly 60% around the minihalo itself. The shock front has mixed in some metals and molecular hydrogen has formed along this front, most notably along the periphery of the minihalo and along accretion lanes. The minihalo begins to cool more efficiently due to molecular cooling.

At 9 Myr, the shock has propagated around the now collapsed minihalo. What remains of the minihalo is enriched to roughly 2% of the value of the incoming material, or $2.5 \times 10^{-3} Z_{\odot}$, and it contains a significant amount of molecular hydrogen. The minihalo begins to cool below 10^3 K . Finally, by about 13 Myr, the shock has passed through the box, leaving a stream of material that is not entirely bound to the x -axis. This is because anisotropies in the minihalo lead to mismatched times at which the shock reaches the antipodal point, resulting in some material being pushed away from the axis. This is different from what is seen in GS10, GS11A and GS11B. This material is almost uniformly at a few 100 K, enriched to 3% of the shock’s metallicity, and has a mass fraction of H_2 of about half a percent. During this time, we find that the dark matter of the minihalo does not respond to the outflow, although it does move in towards the halo from the outer edges of the simulation volume. This is mostly due to our choice of isolated boundary conditions, and results in a small increase in the gravitational attraction on the gas, but this movement is small and well beyond the virial radius of the halo.

After determining the gas that is transferred to the ballistic particle scheme, we find only 24% of the baryonic mass of the original minihalo is contained in these particles, while 76% is blown away from the minihalo, out of the simulation volume. This material is not bound to the x -axis, and does not coalesce into large clumps. For our fiducial case, we consistently get 24% of the mass in particles, regardless of the number of ballistic bins, the density cutoff, or the timescale over which the gas must

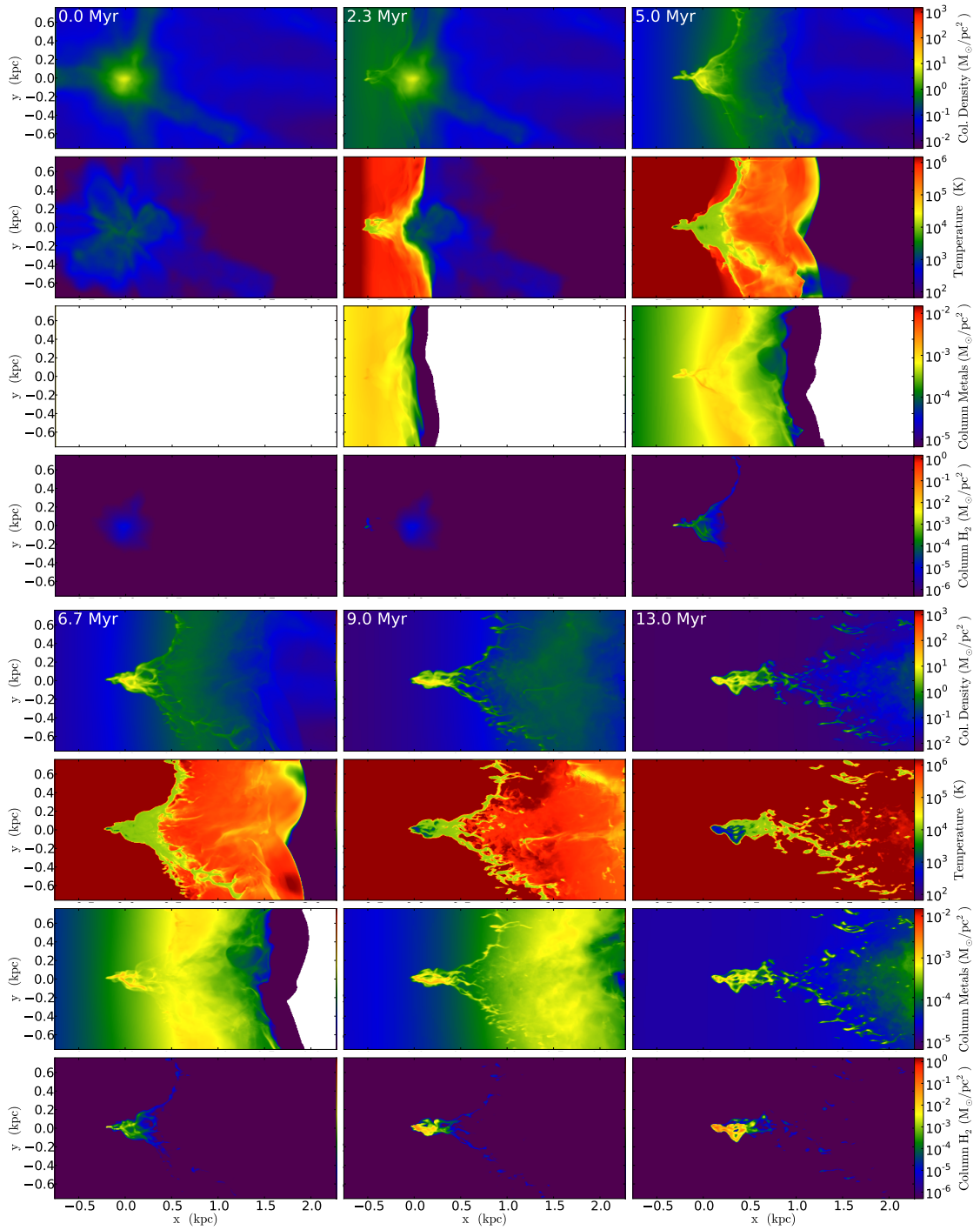


FIG. 4.— Evolution of the fiducial simulation, showing column density (first and fifth row), projection of density-weighted temperature (second and sixth row), the column density of metals (third and seventh row), and the column density of molecular hydrogen (fourth and eighth row) at 0, 2.4, 5.0, 6.7, 9.0, and 13 Myr from left to right.

be bound to the x -axis.

Figure 5 shows the final particles whose masses are above 1% of the original minihalo’s baryons, a limit we adopt in similar figures below. The momentum from the outflow pushes this mass out of the dark matter halo, while small variations in the velocity of the original particles, along with their self-gravity, allow the particles to merge, leading to a small population of high-mass clusters. For the fiducial case, most final particles are about $1\text{--}4 \times 10^4 M_{\odot}$, and have a velocity profile nearly following a free expansion law, with $v \simeq 4.6(x/\text{kpc}) \text{ km s}^{-1} \simeq x/200 \text{ Myr}$, as expected. We also found a slight trend of increasing metallicity with position, due to increased mixing on the backside of the minihalo.

3.2. Convergence

Simulations LR and HR were run with the maximum resolution in FLASH3.2 at half and double that of run FID (11.8pc and 2.46 pc, respectively). In the LR there are regions that do not meet the Truelove criterion (Truelove et al. 1997), as the Jeans length is not resolved by at least four fluid elements. However, in both the FID and HR runs, this criterion is always met. Figure 6 shows the evolution of the column density for the LR, FID, and HR runs. The increased resolution is able to better resolve the fragmentation of the cloud caused by turbulence along the shock front. This increased fragmentation leads to increased metal enrichment and general mixing of the material. Note that unlike GS11A we do not include a subgrid turbulence model in our calculations, meaning that the enrichment we compute is resolution dependent and should be considered a lower limit.

We also performed the same ballistics evolution for each of the simulations. We compare the resulting particles in Figure 7. The amount of the minihalo baryons captured in these particles is 19%, 24%, and 26% for the LR, FID, and HR runs, respectively. The increased resolution has led to more fragmentation, leading to slightly increased enrichment of the final particles with a slightly larger dispersion, and whose mass is in a few more less massive clumps. However, the mass dispersion is roughly 0.3 dex for all three simulations, while the average mass varies only by about 0.06 dex. Thus our statistics are still robust, even if the individual clumps are not identical with their higher resolution counterparts. Likewise, we find little dependence on the abundance of the final clumps, in their evolution, so we do not expect the slightly-increased enrichment at higher resolution to influence our results. See §3.3.5 and §4.2 for more discussion on this. We are thus satisfied that the FID resolution is sufficient to model this interaction for other parameters sets.

3.3. Parameter Study

The simulations run in this parameter suite are detailed in Table 1, with names corresponding to the parameter that was altered from the fiducial value. PO1 has the outflow propagating through the IGM before striking the minihalo, while in all other simulations the outflow propagates along a filament. In the following subsections we discuss both the results from the FLASH3.2 simulations for each parameter as well as the evolution of the ballistic particles.

3.3.1. Minihalo Mass

The minihalo mass is one of the most important parameters, as it sets not only the mass of baryons present, but the scale of the interaction, the virial temperature of the minihalo, and the depth of the gravitational potential. How this parameter affects the evolution of the interaction is shown in Figure 8. Each minihalo is unique, chosen for its mass. Nevertheless, the interactions of the outflows with these minihalos are consistent. We see that the more massive minihalos create denser shock fronts as the outflow is stalled by the denser material, have denser ribbons of material after the shock overtakes the minihalo, and they have larger wakes of swept up material. The nature of the filament along which the outflow propagates appears to influence how the shock interacts with the minihalo itself, and in §3.3.2 we explore whether this can affect the produced particle clouds.

Figure 9 shows the distribution of cloud particles 200 Myr after these simulations. As the minihalo mass increases, the cloud particles are found closer to the dark matter halo, there are more final particles, and they have larger masses. The more massive minihalos have a deeper potential well, and the innermost, most massive cloud particles are unable to escape for the very largest minihalo. One exception to this appears to be PM7. We suspect in this case the proximity of two smaller minihalos, as well as the orientation of a second filament directly behind the minihalo allows the gas to better escape the minihalo, while entraining the secondary filament material. We find the percent of the original minihalo’s baryons in bound cloud particles is much larger for larger minihalo mass, with only 3.7% of baryons contained in the collapsed gas for PM07, while 61% of baryons are contained in PM19.

The metallicity again increases with increasing position of the final cloud particles. The smaller mass minihalo results in less metals penetrating into the cloud, as the shock travels more quickly around the more tenuous material. The relative spread in metallicity, σ_Z/Z , is mostly below 0.1 dex, except for PM19, whose increased gravity allows for more material of different enrichment to be constrained in the final ribbon of material.

3.3.2. Orientation

A key component to anisotropic minihalos in this interaction is how the outflow is oriented with respect to the minihalo and its accretion lanes. Simulation PO1 looks at the effect of orientation on the shock-minihalo interaction. Figure 10 compares the evolution of the fiducial run with that of PO1, which has the outflow propagating through the low-density IGM, instead of along a filament. In FID, the shock material in the filament is stalled, first collapsing the filament gas, before striking the minihalo. In PO1, the shock material along the x -axis is first to hit the minihalo, without a reduction in kinetic energy. The specifics of this interaction will be fairly stochastic, dependent on the orientation of other filaments, and the geometry of the minihalo. In PO1, we find the outflow triggers some molecular hydrogen formation in surrounding filaments, that cool and collapse, while being driven down towards the x -axis. Also, the minihalo baryons are in a more extended and bound ribbon of material at the end of the interaction.

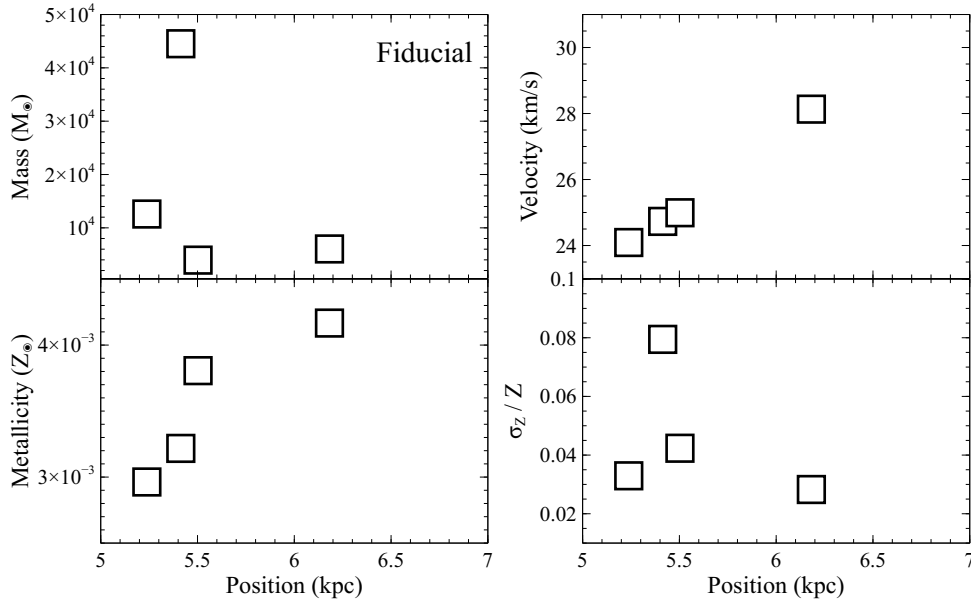


FIG. 5.— Distribution of cloud particle masses (top left), velocity (top right), metallicity (bottom left) and relative metallicity dispersion (bottom right) vs particles positions after 200 Myr for the fiducial run.

In Figure 11 we show the ballistic particles after 200 Myr of evolution for the two different orientations. PO1 has only 14% of the minihalo’s baryons in these particles, compared with FID’s 24%. PO1 has its final particles much further out than FID, due to the undiminished kinetic energy of the outflow. PO1 also has more final particles of lower mass, suggesting that they are less efficient at merging. Regardless of orientation, metallicity increases with position outside the dark matter potential.

3.3.3. Shock Velocity

The shock velocity, v_s , is one of the most significant parameters affecting this interaction. The outflow acts to remove the baryons from their dark matter potential well, sets the post-shock temperature, and catalyzes H_2 and HD formation by ionizing the gas. Figure 12 compares the evolution of the runs with different v_s values.

As the velocity of the shock increases, the post shock density decays quicker to maintain a constant surface momentum. At slower speeds, the minihalo baryons are slowly pushed back. The material does not get constricted to the x -axis, and instead forms a diffuse bow shock, with very little able to collapse or escape the dark matter potential. At intermediate velocities, the material collapses into extended ribbons on the x -axis, with the length of this ribbon decreasing with increasing velocity. At the largest velocity, the most material is collapsed into a single dense clump, with a diffuse envelope of gas.

In Figure 13 we show the ballistic particles after 200 Myr for the simulations that vary the shock speed. The slower outflows are unable to push the gas far from the dark matter potential, imparting little kinetic energy into the gas. As a result, these clumps are also less able to merge, resulting in more numerous cloud particles. The slower the outflow, the longer the timescale of the interaction, which leads to an increase in the enrichment of the baryonic material in the slow velocity cases. The most energetic outflows, on the other hand, are unable to appreciably enrich the baryons efficiently, which both lowers the average metallicity of the clumps and increases

the metallicity dispersion of individual cloud particles. Finally, in Pv75 roughly 36% of the minihalo baryons are contained in the final cloud particles. In Pv125, only about 8% of the baryons are in these particles, and then for even larger speeds we asymptote to about 25%. At the lowest shock speed, the material is not efficiently removed from the halo. At somewhat larger velocities the material is stripped from the minihalo potential, while not collapsed on to the x -axis. At even higher shock speeds, the material is collapsed on to the x -axis before it can be quickly removed from the potential, leading to a higher baryonic component.

3.3.4. Outflow Surface Momentum

The shock surface momentum is a significant parameter that along with the shock velocity, sets the initial energy driving the outflow, while simultaneously setting the surface density of the post-shock material. Figure 14 compares the evolution of the runs with different μ_s values. As the surface momentum of the shock increases, so does its surface density, leading to increased momentum transfer to the minihalo gas. This leads to increased fragmentation of the shock front, and confinement onto the x -axis. At the lowest surface momentum, the final ribbon of material is more extended perpendicular to the x -axis, and less extended along the x -axis. At the largest surface momentum, the final ribbon of material is the opposite, more constrained to the x -axis, and more extended along the x -axis.

In Figure 15, we show the ballistic particles after 200 Myr of evolution for the simulations that vary the surface momentum. The position of most of the final cloud particles is roughly the same for all surface momenta, indicating a greater dependence on the shock speed. Nevertheless, the smallest and largest momentum cases have final particles further removed from the dark matter potential. The primary cause of this in the low momentum regime is that more gas is bound to the x -axis at further distances, leading to larger clumps further away from the dark matter potential. Note that P μ 3 has 28% of

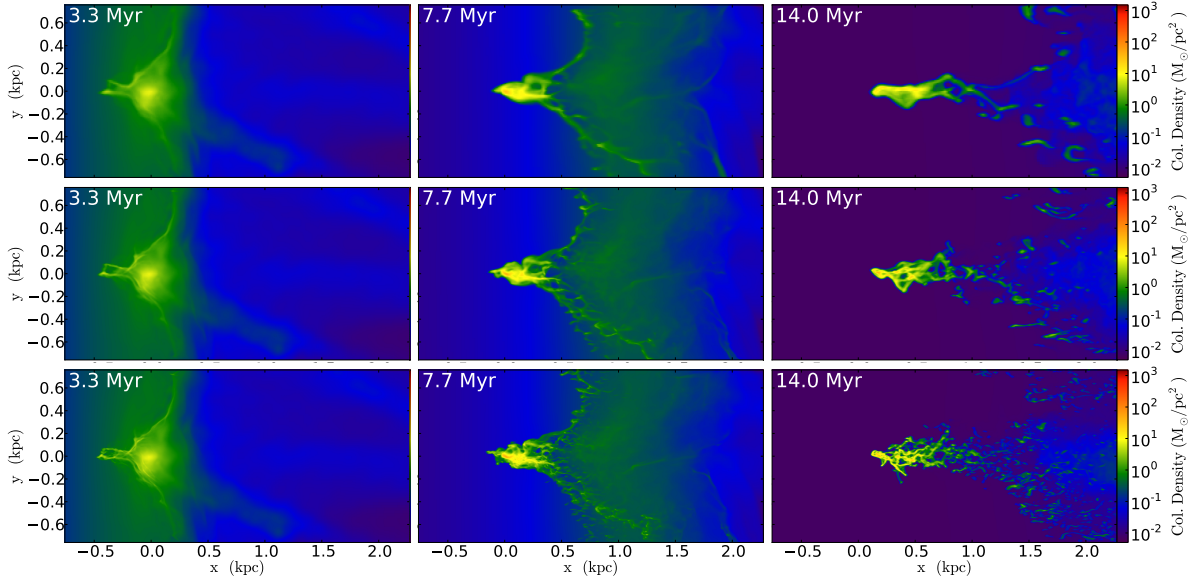


FIG. 6.— Demonstration of convergence of the fiducial simulation (FID; center) with the low-resolution (LR; top) and the high-resolution (HR; bottom) column density results at 3.3, 7.7, and 14 Myr from left to right.

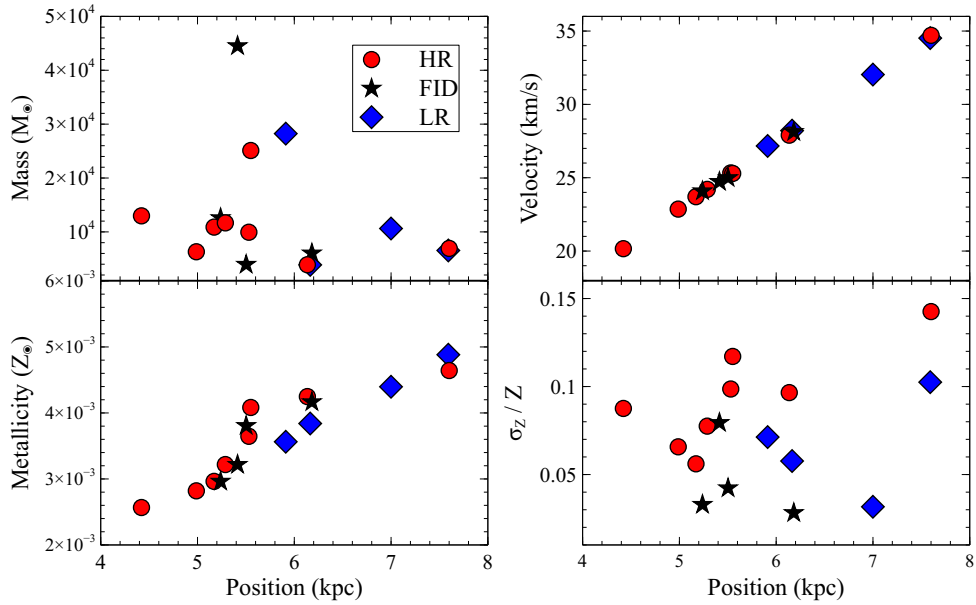


FIG. 7.— A comparison between the LR (blue diamonds), FID (black squares), and HR (red circles) particle masses (top left), velocity (top right), metallicity (bottom left) and metallicity dispersion (bottom right) vs particles positions after 200 Myr.

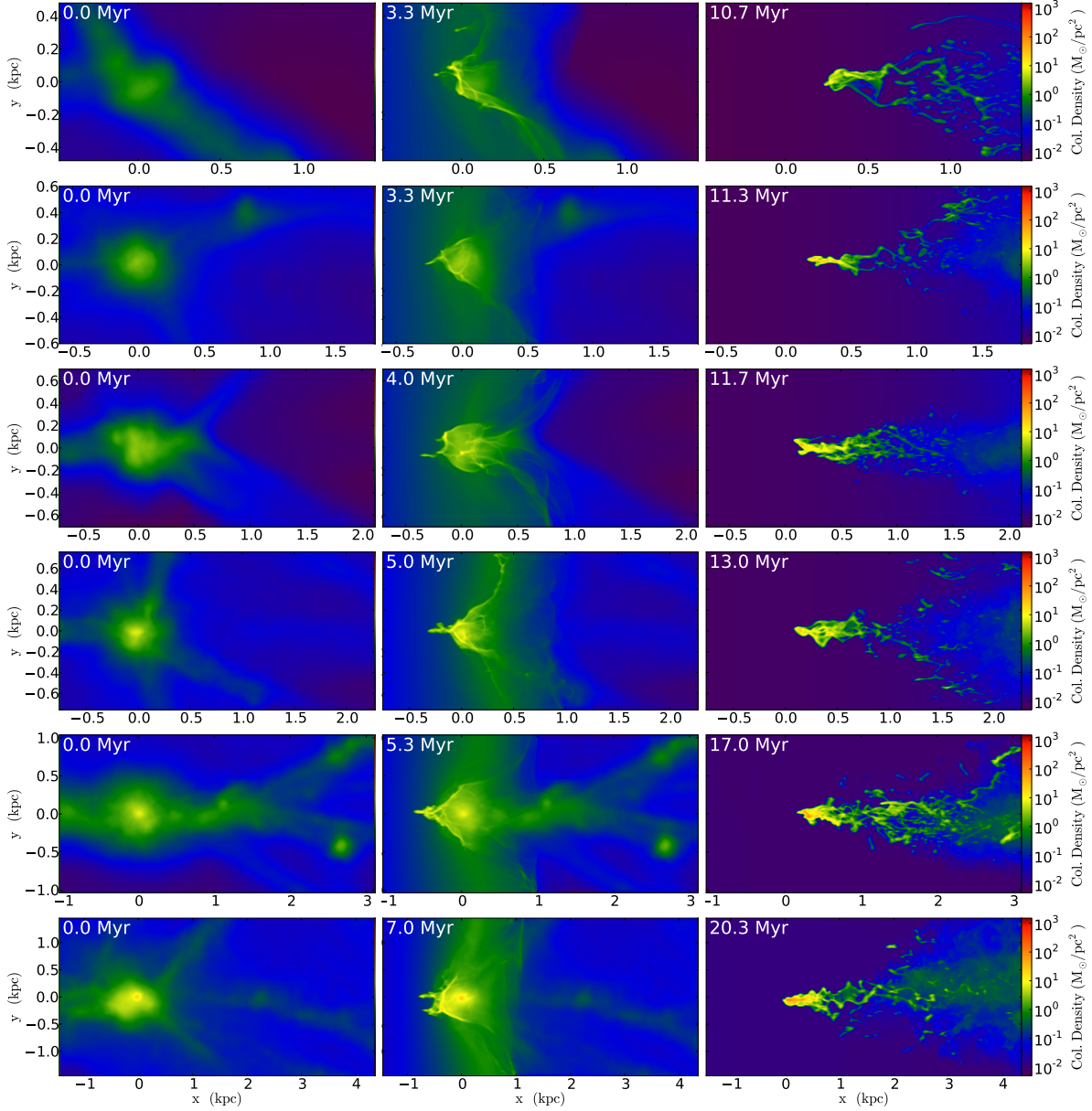


FIG. 8.— Column density of the simulations varying the minihalo mass, from top to bottom PM07, PM1, PM23, FID, PM7, and PM19, respectively, with evolution increasing from the beginning on the left, to when the outflow is just passing the minihalo in the middle, to when the outflow reaches the end of the box on the right.

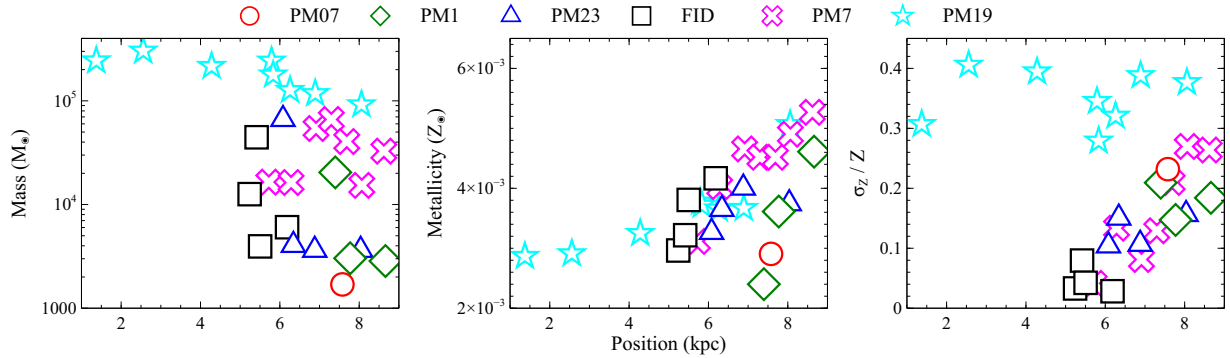


FIG. 9.— Comparison between the PM07 (red circles), PM1 (green diamonds), PM23 (blue triangles), FID (black squares), PM7 (magenta crosses) and PM19 (cyan stars) simulations illustrating the dependence on minihalo mass. The particle masses (left), metallicity (middle) and relative metallicity dispersion (right) vs particles positions, after 200 Myr are shown. With larger momentum, less gas is ultimately bound to the x-

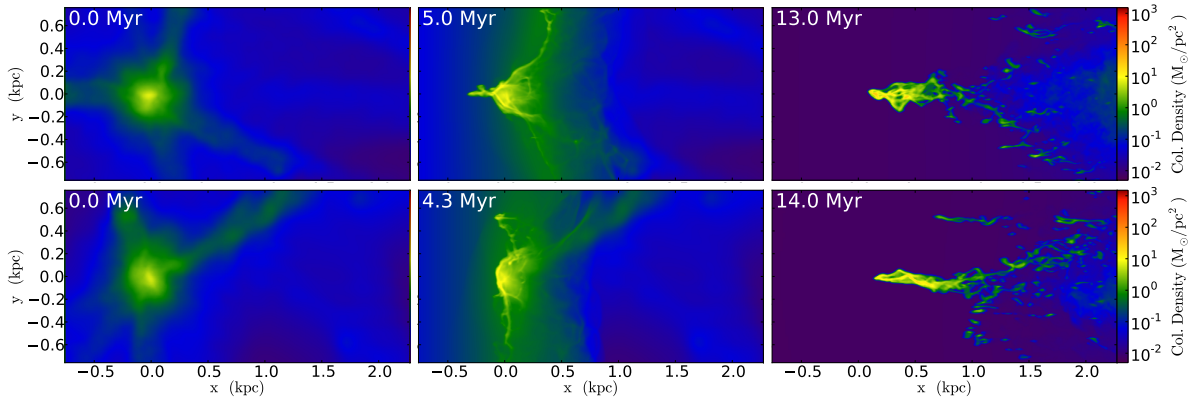


FIG. 10.— Column density of the simulations varying the minihalo-shock orientation, with FID on top, and PO1 on bottom, and evolution increasing from the beginning on the left, to when the outflow is just passing the minihalo in the middle, to when the outflow reaches the end of the box on the right.

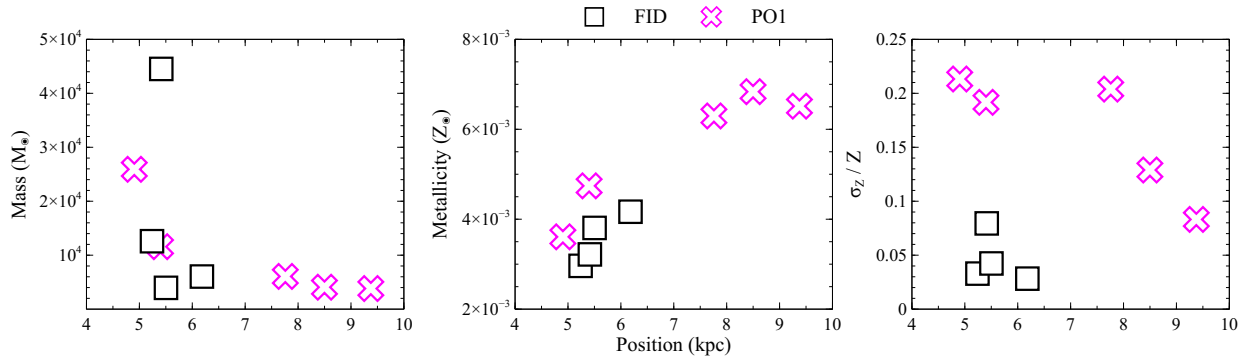


FIG. 11.— Comparison between the PO1 (magenta crosses) and FID (black squares) simulations illustrating the dependence on minihalo-shock orientation. The particle masses (left), metallicity (middle) and relative metallicity dispersion (right) vs particles positions after 200 Myr are shown.

axis at further distance, despite the ribbon of material being initially more extended. P μ 9 has about 24% of the minihalo baryons in the final cloud particles. Since we only show the final particles with more than 1% of the baryon component, there are many more extended particles for intermediate momentum that are not shown. The mass of the final cloud particles is roughly independent of momentum. Again, the total mass is highest at lowest momentum. The enrichment of these clouds again scales with position, for a given simulation, and increases with momentum, as does the dispersion. This is due to the increased fragmentation and confinement of the baryons along the x -axis at larger momentum, leading to a higher penetration of enriched material.

3.3.5. Outflow Abundance

Throughout the simulations described above, the level of enrichment of the final minihalo material has been consistently a few percent of the outflow abundance. Thus by changing the outflow abundance, we expect the enrichment of the minihalo baryons to vary, which may affect its cooling efficiency as well as the metallicity of the final clusters where stars will be formed. Note that since the majority of the cooling is caused by the produced molecules, the increased metallicity may have little effect on the evolution. We explore this evolution in Figure 16. We see no discernible difference between the different models, with the exception of PZ5. The most enriched outflow, once a significant amount of met-

als has mixed into the minihalo, is able to contribute a non-negligent amount of cooling from metals, leading to a more collapsed structure starting at 7.7 Myr, and much more noticeable by 13 Myr. Also, the post-shock ambient medium is able to cool more, and fragments earlier than the metal-poor runs.

In Figure 17, we show the ballistic particles after 200 Myr of evolution for the simulations that vary the outflow abundance. The mass distribution of final particles is almost independent of enrichment. Only in the most enriched outflow is the additional cooling sufficient to cause increased fragmentation in the pre-ballistic gas, such that these clumps do not merge. In all simulations roughly 25% of the minihalo baryons are bound in these cloud particles. The enrichment appears to only affect the abundance of the clumps, which is always roughly 2% of the outflow abundance, with a slight dependence on position of the final particles. The variance in abundance is fairly uniform, although the most metal-rich outflow has a slight peak in its spread. This simulation's increased fragmentation leads to a larger variance of enriched proto-clumps, which, through merging, results in clumps with higher variance.

3.3.6. Redshift

The redshift of the interaction is a significant parameter that sets the minihalo density and temperature profiles, as well as its environment. The redshift also sets the post-shock density as well as the surface momentum.

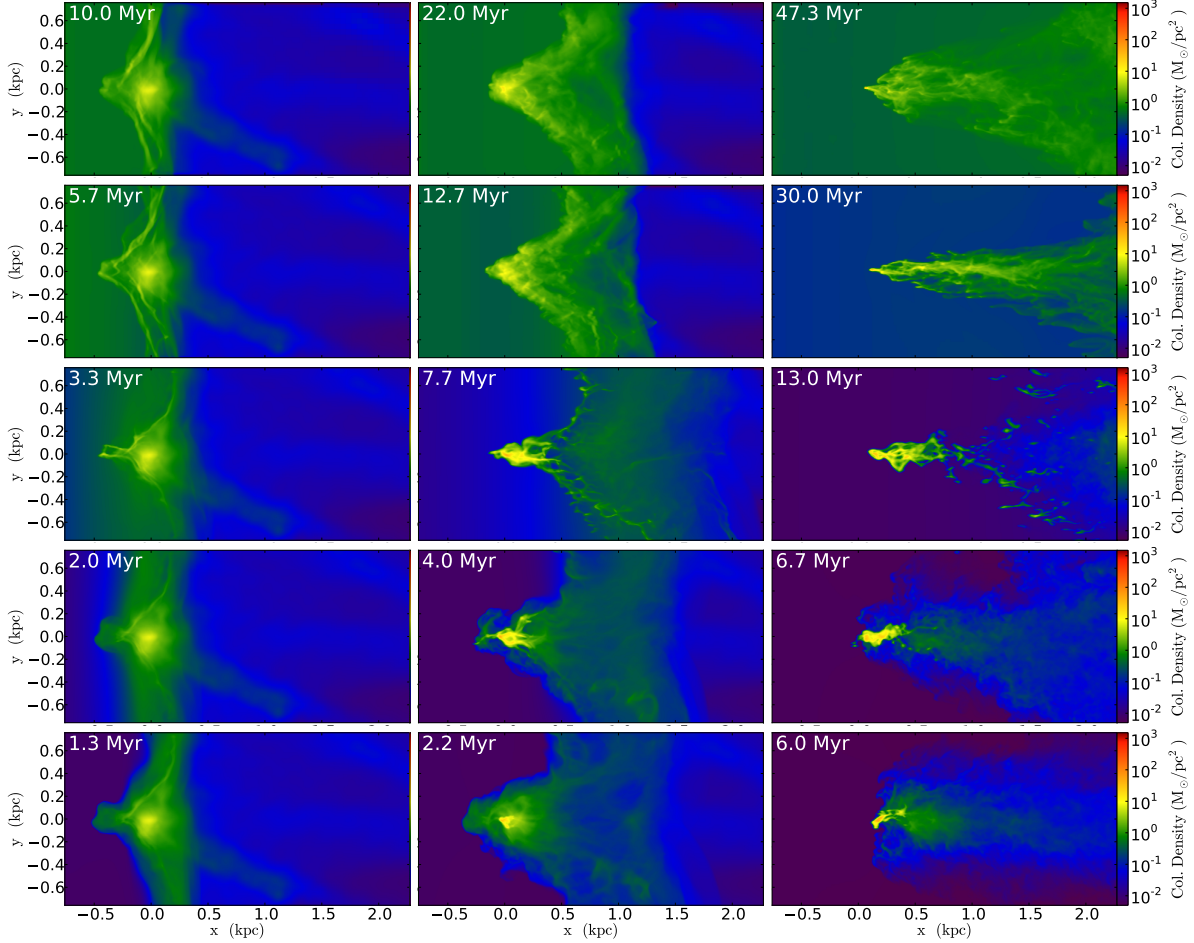


FIG. 12.— Column density of the simulations varying the shock velocity, v_s , with Pv75, Pv125, FID, Pv340, and Pv510 from top to bottom, and evolution increasing from the first interaction with the minihalo on the left, to when the outflow is just passing the minihalo in the middle, to when the outflow reaches the end of the box on the right.

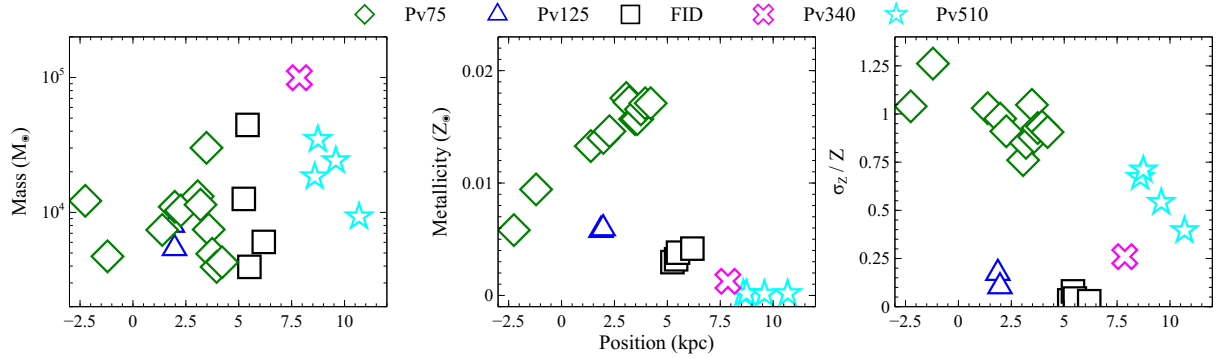


FIG. 13.— Comparison between the Pv75 (green diamonds), Pv125 (blue triangles), FID (black squares), Pv340 (magenta crosses), and PE30 (cyan stars) simulations illustrating the dependence on shock velocity. The particle masses (left), metallicity (middle) and relative metallicity dispersion (right) vs particles positions after 200 Myr are shown.

We assume the surface density scales with $(1+z)^2$, while the shock velocity is invariant with redshift, as it scales with the supernovae input energy, which we assume is independent of redshift. In Figure 18 we illustrate the evolution of this interaction for various redshifts, while scaling the color scheme with $(1+z)^2$. We see little variation between the three simulations. The timescale of the interaction scales with $(1+z)^{-1}$ since v_s is the same, while the physical scale of the minihalo is smaller by

$(1+z)$. The cooling is more efficient at higher redshifts with larger densities, leading to slightly cooler, denser clumps, however this effect is minor.

In Figure 19, we show the ballistic particles after 200 Myr of evolution for these simulations. Similar to the metallicity parameter study, we see subtle effects. The increased cooling at the largest redshift leads to an increase in fragmentation of the clumps before the ballistic evolution, and this increased fragmentation leads to less

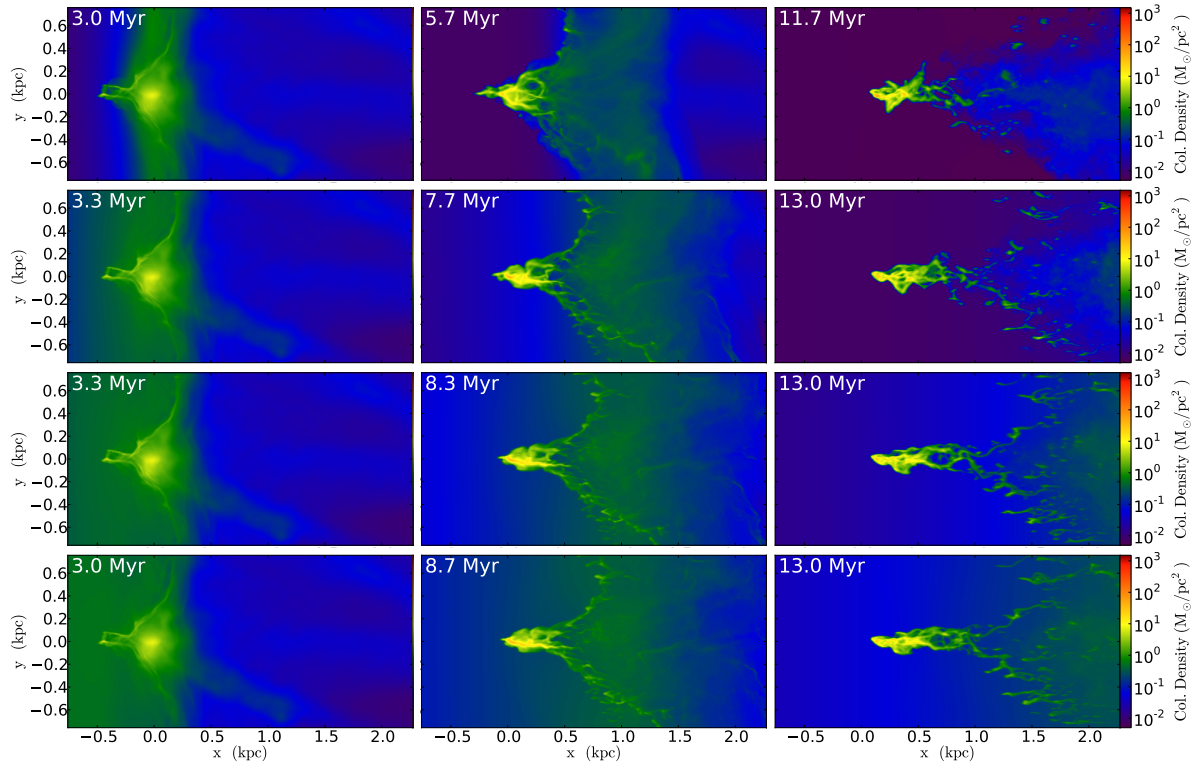


FIG. 14.— Column density of the simulations varying the shock surface momentum, μ_s , with $P\mu 3$, FID, $P\mu 8$, and $P\mu 9$ on from top to bottom, and evolution increasing from the first interaction with the minihalo on the left, to when the outflow is just passing the minihalo in the middle, to when the outflow reaches the end of the box on the right.

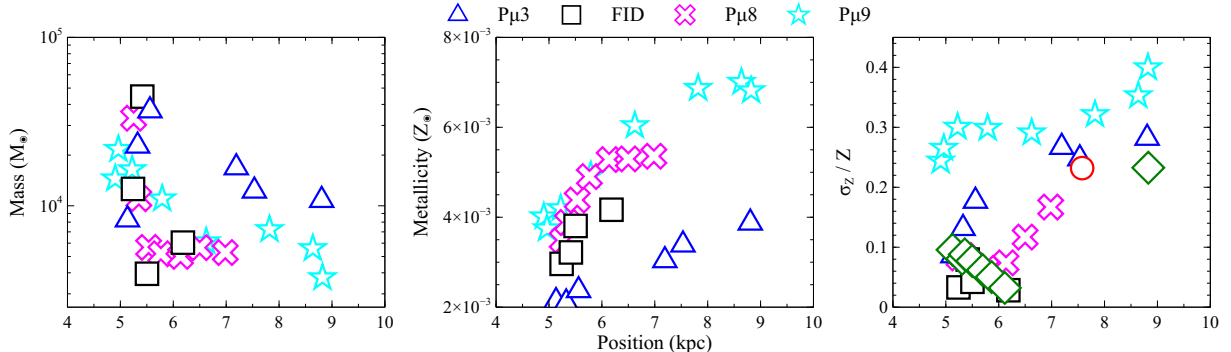


FIG. 15.— Comparison between the $P\mu 3$ (blue triangles), FID (black squares), $P\mu 8$ (magenta crosses), and $P\mu 9$ (cyan stars) simulations illustrating the dependence on shock surface momentum. The particle masses (left), metallicity (middle) and relative metallicity dispersion (right) vs particles positions after 200 Myr are shown.

merging between the final cloud particles and an increase in enrichment and enrichment variance.

4. OBSERVATIONAL SIGNATURES

Our various simulations of starburst-driven outflows interacting with minihalos consistently produce dense massive objects that we expect to form stars since molecular cooling should be sufficient to cool these objects beyond the Jeans limit. While the resulting high-redshift cluster of stars are not observable with modern telescopes, their epoch of star formation should generate sufficient UV flux and Lyman- α photons that they may be visible with upcoming observatories. Also, their compact nature should be sufficient to survive to modern day, such that we may be able to identify presently existing objects to compare with these clusters. Here we discuss both of

these possibilities.

4.1. Direct Observations

To determine how bright the star-formation episode in our simulations would appear, we produced mock observations of these interactions. As we did not implement a star formation prescription in the simulations themselves, we implemented the post-processing technique of GS11B. We broke the forming ribbon of collapsed material in 175 stellar mass bins. Inside each bin we added the mass from cells with density above $([1+z]/9)^3 \times 10^{-23} \text{ g cm}^{-3}$, consistent with GS11B and the typical peak density of the ribbon. This assumes a star-formation efficiency of 100% for gas above this threshold, thus our estimates are upper limits. We interpolated this stellar mass from one output to the next, yielding an effective

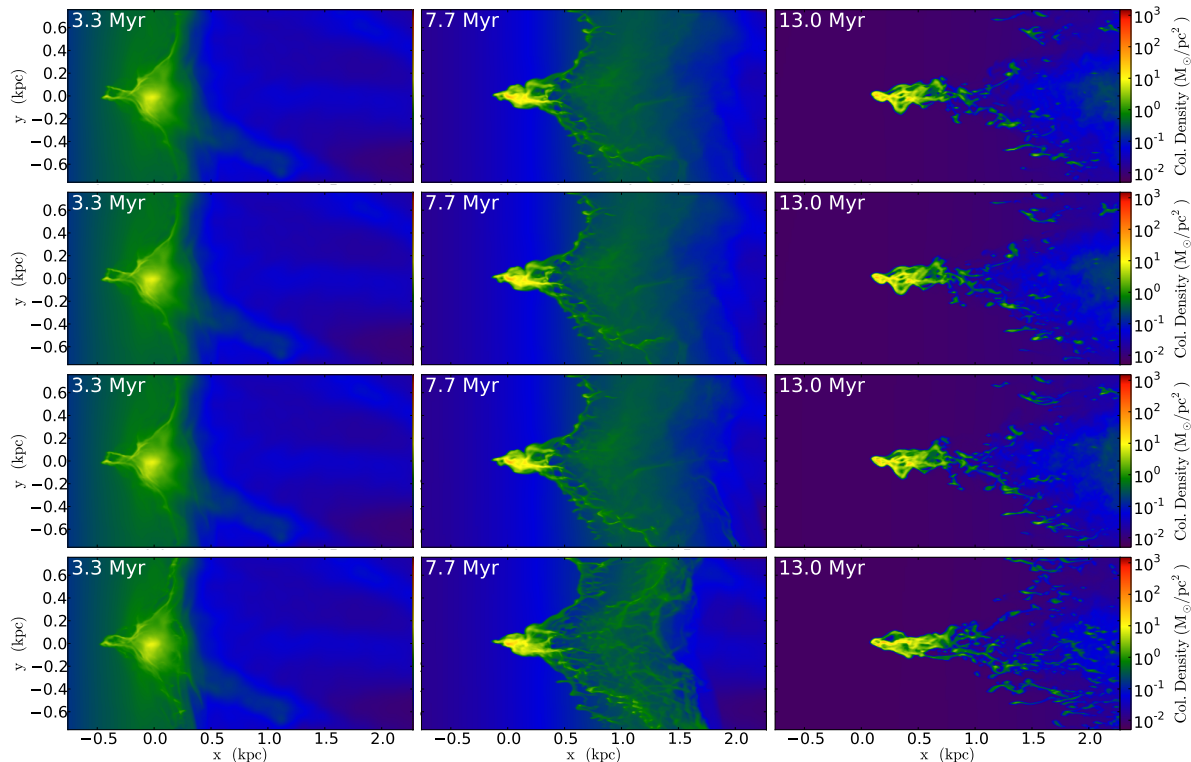


FIG. 16.— Column density of the simulations varying the shock enrichment, with PZ005, PZ05, FID, and PZ5 from top to bottom, and evolution increasing from the first interaction with the minihalo on the left, to when the outflow is just passing the minihalo in the middle, to when the outflow reaches the end of the box on the right.

star-formation history over the ribbon. We used the stellar population synthesis code bc03 (Bruzual & Charlot 2003) to estimate fluxes from a starburst population, and convolved these outputs with our ribbon’s star-formation history as a function of frequency and age. We were also able to make estimates on the Lyman- α , H- α and H- β lines by assuming a production of Ly α photons proportional to the star formation rate, while the Balmer lines were estimate from case B (Osterbrock 1989). For more details the reader is referred to GS11B.

We determine the fluxes expected in each of the *James Webb Space Telescope* (*JWST*) bands, as well as from bright line emission that may be detected with future ground-based observing facilities, such as the *Giant Magellan Telescope* (*GMT*), the *Thirty Meter Telescope* (*TMT*), and the *European Extremely Large Telescope* (*E-ELT*). The expected F115W wideband filter detections and expected observed Ly α flux are presented in units of per ribbon length in Figure 20 for several parameters. The physical and angular scales both assume an edge-on viewing angle. Note that for the redshift parameter study, there is not a constant mapping between position and observed angle, thus we have set the x -axis to reflect the angular scale. We find that the final ribbon of material is typically a fraction of a kpc long, slightly smaller than those found in GS11B. This is not surprising, as the unidealized environment, including filaments, makes it more difficult for an efficient transfer of kinetic energy from outflow to minihalo gas. We tabulate the integrated flux from all bands for each simulation in Table 2. Note that this is the net flux from the star formation episode, and not the expected flux from the final globular cluster-like clouds.

We find that the expected flux in the *JWST* bands is typically around 1 nJy/kpc, or just under 1 nJy when integrated over the entire ribbon, with this flux greatest in the F115W band. These values are slightly below those of GS11B, and thus are not very optimistic for detection by *JWST*, as typical observations with *JWST* will have sensitivity down to only 10-20 nJy for a 10σ detection after a 10,000s integration (Stiavelli et al. 2008).

Fortunately, the expected fluxes from Ly α , although a factor of a few less than those predicted in GS11B, are still well above the expected detection limit of upcoming ground-based observing facilities. For example, the proposed *Near Infrared Multi-object Spectrograph* on the *GMT* is expected to find similar sources down to a flux limit of 10^{-20} erg cm $^{-2}$ s $^{-1}$ given 25 hr of integration (McCarthy 2008; GMT Science Case). Also, the *Infrared Imaging Spectrometer* on the *TMT* will detect Ly α sources at $z = 7.7$ with fluxes of 10^{-18} erg cm $^{-2}$ s $^{-1}$ with a signal-to-noise ratio of 15 in only 1 hr of integration (Wright & Barton 2009; TMT Instrumentation and Performance Handbook). Finally, the planned *Optical-Near-Infrared Multi-object Spectrograph* for the *E-ELT* will detect sources with fluxes of 10^{-19} erg cm $^{-2}$ s $^{-1}$ with a signal-to-noise ratio of 8 in 40 hr of integration (Hammer et al. 2010). All three of these detectors would be sufficient to observe the brightest of our objects.

These future ground-based observatories will employ the use of adaptive optics, hoping to get angular resolution in the range of 0.1-0.3 arcsec (McCarthy 2008; Wright & Barton 2009; Hammer et al. 2010), which means our objects will likely be unresolved. However, using Equation (4) many should be within roughly 5 kpc of the starbursting galaxy driving the outflow, with masses

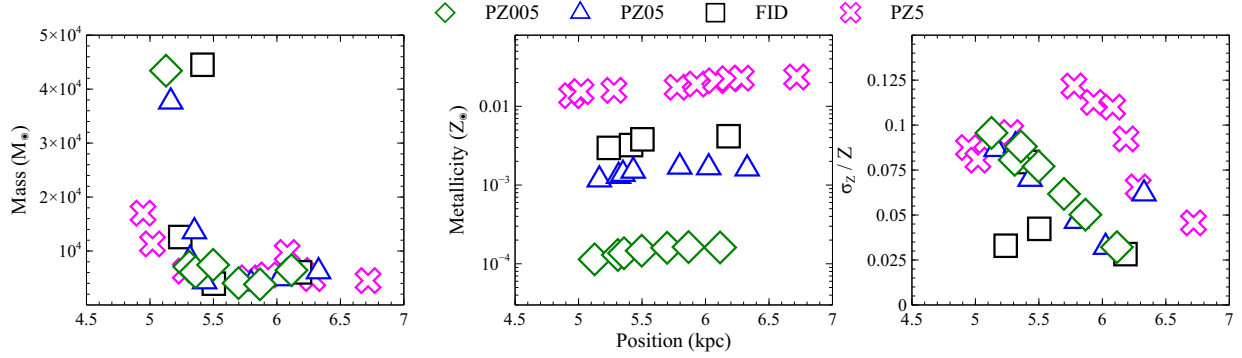


FIG. 17.— Comparison between the PZ005 (green diamonds), PZ05 (blue triangles), FID (black squares), and PZ5 (magenta crosses) simulations illustrating the dependence on shock metallicity. The particle masses (left), metallicity (middle) and relative metallicity dispersion (right) vs particles positions after 200 Myr are shown.

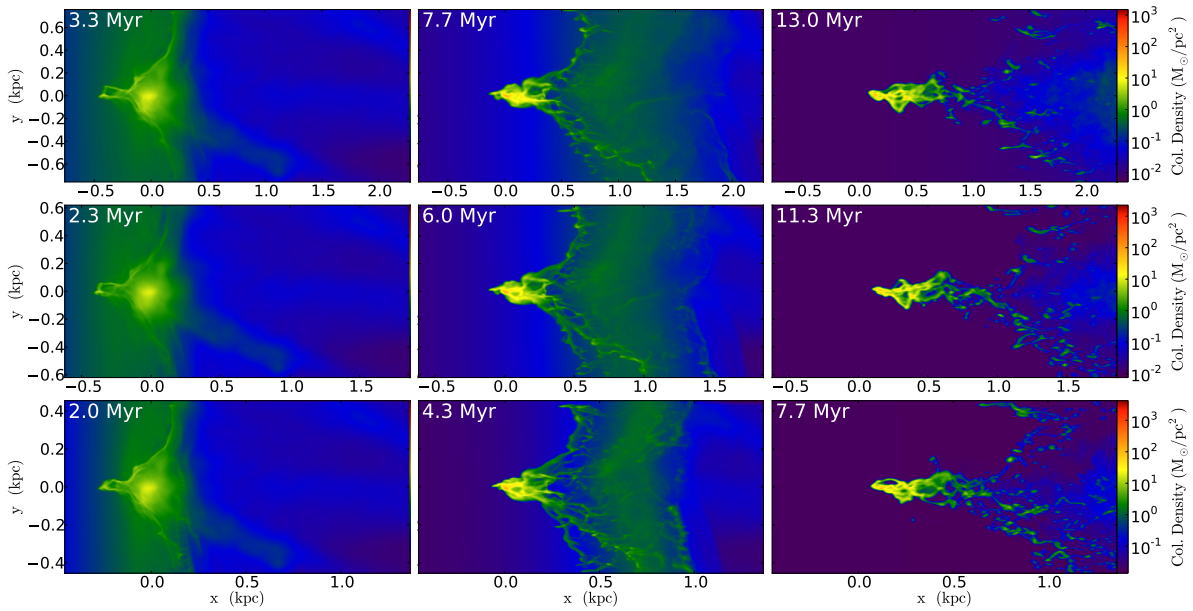


FIG. 18.— Column density of the simulations varying the redshift of the interaction, along with the surface density, with FID, Pz10C, and Pz14C, from top to bottom, and evolution increasing from the first interaction with the minihalo on the left, to when the outflow is just passing the minihalo in the middle, to when the outflow reaches the end of the box on the right.

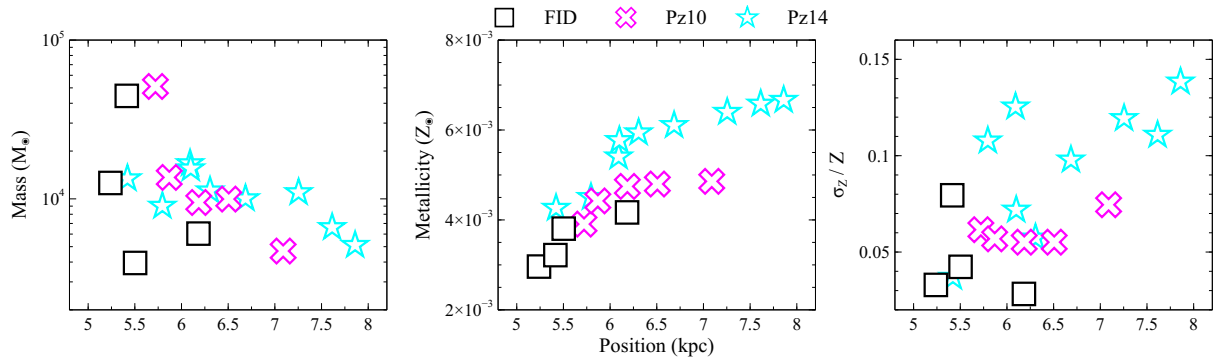


FIG. 19.— Comparison between the FID (black squares), Pz10 σ (dark blue circles), Pz10C (blue triangles), and Pz14C (magenta crosses) simulations illustrating the dependence on redshift. The particle masses (left), metallicity (middle) and relative metallicity dispersion (right) vs particles positions after 200 Myr are shown.

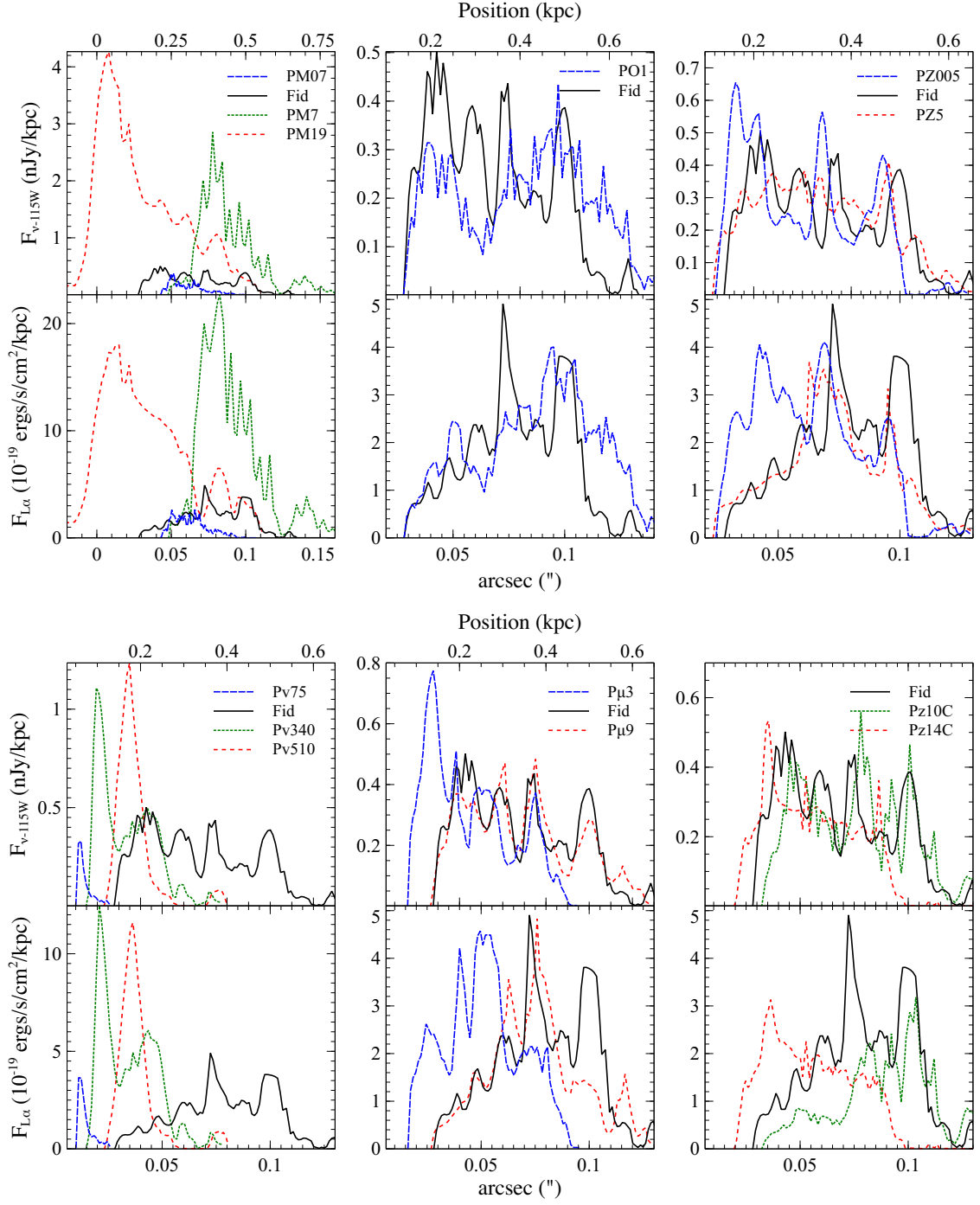


FIG. 20.— Comparison between the mock observations of several of our simulations as seen in the F115W wideband filter of *JWST* (first and third row), and observed Ly α (second and fourth row). We illustrate the effect of different parameters in columns, with minihalo mass, shock orientation, shock enrichment, shock velocity, shock surface momentum, and redshift, running from top left to bottom right, respectively.

TABLE 2
OBSERVED FLUX

Simulation	F115W (10^{-2} nJy)	Ly α (10^{-20} erg cm $^{-2}$ s $^{-1}$)	Extent (kpc)	Extent (")
FID	11.9	8.83	0.766	0.155
PO1	11.3	10.9	0.871	0.176
PM07	2.90	2.80	0.460	0.0928
PM1	7.71	7.52	0.529	0.107
PM23	9.33	5.38	0.710	0.143
PM7	37.7	39.2	1.44	0.292
PM19	95.7	52.4	0.747	0.151
Pv75	0.866	1.02	0.169	0.0341
Pv125	2.87	2.55	0.962	0.194
Pv340	9.47	10.6	0.362	0.0731
Pv510	7.26	7.01	0.393	0.0793
P μ 3	11.4	8.62	0.492	0.0993
P μ 8	12.1	8.05	0.610	0.123
P μ 9	11.3	7.74	0.616	0.124
Pz10	9.51	4.73	0.652	0.152
Pz14	6.16	4.20	0.472	0.140
PZ005	12.3	9.66	0.625	0.126
PZ05	12.1	9.00	0.613	0.124
PZ5	12.2	7.46	0.689	0.139

$\gtrsim 10^8 M_{\odot}$, which will be easily detectable with *JWST* broadband data. Thus we expect that future observations of starbursts with ground-based narrowband imaging may see barely resolved objects around the periphery of starburst galaxies extended away from the central starburst galaxy.

Finally, the observability of these objects are not very dependent on our parameters. The notable exceptions are minihalo mass and shock speed. For large minihalo masses, there are significantly more photons emitted for larger mass. This is because the high-mass runs result both in significantly more collapsed baryons and higher densities, leading to increased cooling and collapse. Similarly, there are significantly more photons emitted when the shock is faster. This is because the increased shock speed results in more compressed material along the x -axis, leading to denser material, and thus more stars.

4.2. Modern-day Analogs

Figure 21 shows the distribution of final cloud particles whose masses are at least 1% of their minihalo’s baryon mass for all of the simulations performed in this work.

We find that the mass of our final cloud particles range from $\approx 10^{3.5}$ to $10^{5.5} M_{\odot}$, while the metallicity of the final cloud particles are consistent with an asymmetric log-normal distribution of $\log Z = -2.44_{-0.76}^{+0.36}$. Our dispersion in metallicity is typically about 0.06 dex. Our final cloud particles can be as far removed from their dark matter halo as 12 kpc, with the typical particles found removed by about 6 kpc.

The statistical sample of the final cloud-particles from all of our simulations shares many traits with modern day globular clusters. First, the majority of our clusters are unbound from their dark matter halo, consistent with observations of globular clusters which limit the amount of dark matter at less than twice the amount of gas (e.g., Moore 1996; Conroy et al. 2011; Ibata et al. 2013). Also, their enrichment is significantly homogenous, with less than 0.1 dex for most particles. However, there is a tension between the metallicities of our final cloud particles and observations around the Milky Way and Andromeda, which find a consistent value of $\log Z = -1.6 \pm 0.3$ (Zinn 1985; Ashman & Bird 1993). If most starburst outflows

at these high redshifts were more metal-rich than we assume here (cf., Scannapieco et al. 2004), with values of $Z \simeq 0.3 Z_{\odot}$, then our results would be more consistent with these observations. Additionally, we have purposefully neglected to include subgrid turbulent mixing, as we were concerned with overestimating this process. This may also explain why we only found an enrichment of about 2% of the outflow’s metallicity, which may be much lower than actually occurs in this interaction.

Finally, our typical mass of $\sim 10^4 M_{\odot}$ has a large scatter, and although it is below the average mass of halo globular clusters in the Milky Way, with an observed distribution much closer to $\log M = 5.0 \pm 0.5$ (Armandroff 1989), this typical mass is not unreasonable given our fiducial mass. Our process of making globular cluster-like clumps seems most efficient at higher mass, and our largest mass, PM19, produced multiple final particles with masses of a few $\times 10^5 M_{\odot}$. It would be interesting to study this parameter space further around such high-mass minihalos, keeping in mind that provided $M_6 < 52([1+z]/10)^{-3/2}$, then the virial temperature of the halo will be less than 10^4 K, and will be unable to cool on its own. That our objects are typically less massive and less enriched than modern-day globular clusters may be consistent with some observations that show that their metallicity may scale slightly with mass (e.g., Ashman & Bird 1993; Harris et al. 2006, 2009; Mieske et al. 2006; Strader et al. 2006; Peng et al. 2009). Additionally, since structure formation is hierarchical, we would expect a large abundance of smaller mass objects. Destructive processes then act to destroy these smaller clusters. First, the minimum radius as a function of mass is bound by mechanical evaporation (e.g., Spitzer & Thuan 1972). Second, the maximum radius as a function of mass is bound by ram-pressure stripping as the clusters move through the plane of the Galaxy (e.g., Ostriker et al. 1972). Thus, only the largest of these objects should survive to today. Since the destructive processes set the minimum mass of the globular cluster mass distribution for a given age of the host galaxy, we would expect that at higher redshift the globular cluster mass distribution should approach the distribution found in our very high redshift models.

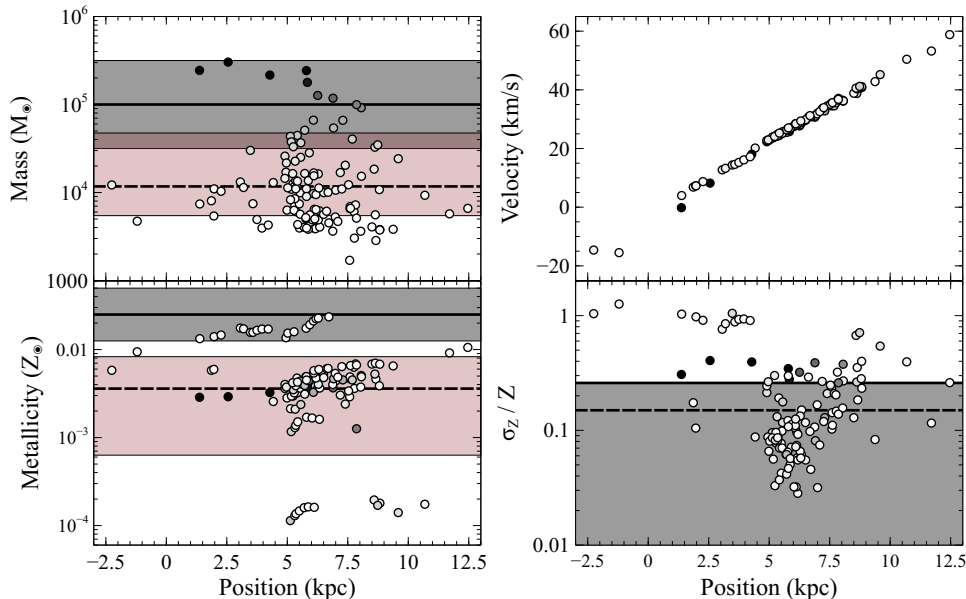


FIG. 21.— The distribution of final cloud particles for all of our simulations. The particle masses (top left), velocity (top right), metallicity (bottom left) and relative metallicity dispersion (bottom right) vs particles positions after 200 Myr are shown. The circles’ color is indicative of the particle mass, darker for more massive particles. The solid lines show the average values for observed halo globular clusters and include a shaded region corresponding to the 1- σ spread in the observations. The dotted line and pink shaded regions mark the asymmetric log-normal distribution of our results.

5. SUMMARY AND CONCLUSIONS

The early Universe hosted a large population of small dark matter ‘minihalos’ that were too small to cool and form stars on their own. These existed as static objects around larger galaxies until acted upon by some outside influence. Outflows, which have been observed around a variety of galaxies, can provide this influence in such a way as to collapse, rather than disperse the minihalo gas.

Here we performed SPH cosmological simulations using the GADGET code to produce realistic minihalos and their environment at $z \simeq 10$. We then implemented a derefinement technique for dark matter particles in the AMR code FLASH. With this we mapped the SPH minihalos into AMR datasets and conducted a parameter suite studying the effect of energetic outflows, similar to those originating from high-redshift starbursting galaxies, impacting inert primordial minihalos. This was a continuation of the idealized work of GS10, GS11A, and GS11B.

We endeavored to determine what effect the minihalo mass, outflow-minihalo environment, outflow speed, outflow surface momentum, outflow metallicity, and redshift had on this interaction. We found that the general interaction proceeded by first shock-heating the front of the minihalo, catalyzing the production of molecular hydrogen. As the shock traversed the rest of the minihalo and molecular hydrogen continued to form, increasing the efficiency of cooling, while simultaneously compressing the minihalo towards the x -axis. The compressed minihalo gas continued to cool courtesy of the molecular hydrogen, while it was pushed out of the dark-matter halo. The shock then dissipated, removing roughly 75% of the baryons from the system, and collapsing the remaining 25% into a cool, relatively homogenous ribbon that was no longer bound to the dark matter halo. To compare, the idealized interaction studied in GS11B found up-

wards of 100% of the baryons condensed into this ribbon. Typically the resulting ribbon of gas was enriched to $\simeq 2\%$ the metallicity of the outflow, and this material was then treated ballistically, allowing for merging between separate clumps.

The most influential parameters are the minihalo mass, orientation, and shock velocity. The minihalo mass is essential in two respects. First, changing this parameter requires changing the particular minihalo and environment mapped from the cosmological simulation. This produced stochastic effects whereby individual minihalo asymmetry and environment influenced the behavior of the interaction as well as its final cluster distribution. This was made clear by comparing models FID and PM2, which varied subtly in mass, but had significantly different shapes and environments. Second, the minihalo mass sets the abundance of gas available to the interaction, as well as the original minihalo temperature and density profile. As the minihalo mass increased in our simulations, more mass collapsed along the x -axis, but less was able to escape the dark matter potential, a trend similar to that found in GS11B.

The orientation is also important as it sets the medium the shock interacts with before striking the minihalo. If an outflow was propagating along a filament, in our simulations, it acted to delay the initial impact, leading to less momentum transfer. Also, this delay allowed the surrounding shock to strike the periphery of the minihalo first, causing it to preferentially collapse before being pushed along out of the halo. Thus, we find that when the shock is oriented along a filament, we have a larger fraction of baryons collapsed into the final cloud particles.

Finally, the shock velocity plays a dramatic role in the interaction. At very low velocities the shocks were incapable of collapsing much of the baryons into a coherent ribbon on the x -axis, leading to a large number of low-

mass, enriched clumps that were still bound to the dark matter potential. As the shock speed increased, baryons were condensed more efficiently, leading to more massive final particles that were more removed from the dark matter potential.

We also produced simulated observations of this interaction using the post-processing technique from GS11B. We find that the final ribbon of material is typically a fraction of a kpc long, slightly smaller than those found in GS11B, and by using Equation (4) can be found around 5 kpc from the starburst galaxy driving the outflow. We find that the expected flux in the JWST bands is typically around 1 nJy/kpc, or just under 1 nJy when integrated over the entire ribbon, well below the expected sensitivity of the telescope. However, we find expected Ly α fluxes of around 10^{-19} erg cm $^{-2}$ s $^{-1}$, well above the expected detection limit of upcoming ground-based observing facilities. Although likely unresolvable, these objects should be visible within 2" of the starburst driving the interaction. Thus future observations of dense bright clumps around the periphery of starburst galaxies will be a clear demonstration of outflows driving star-formation in surrounding minihalos.

Finally, the statistical sample of the final cloud-particles from all of our simulations share many traits with modern day halo globular clusters. They are often unbound from their host dark matter halos by about 6 kpc, but by as much as 12 kpc, and are chemically homogenous. Our mass distribution has a typical value of $10^4 M_{\odot}$ with a large scatter, while the most massive cloud particles have masses of a few $\times 10^5 M_{\odot}$, consistent with modern day halo globular clusters. This indicates that most present-day globular clusters are analogues of the objects created from minihalos with $M_6 \sim 20 - 60$, where we show the production of larger final clumps to be more efficient. Also, the enrichment of our objects is lower than seen in globular clusters. This suggests that a way of modeling subgrid mixing must be included, or

that starburst galaxies may drive winds as enriched as $\sim 0.3 - 0.5 Z_{\odot}$.

We conclude that the interaction of starburst outflows with primordial minihalos is an energetic event that leads to several dense, uniformly-enriched clumps of gas that would be expected to undergo star formation. Such interactions may be visible with the next generation of ground-based telescopes, and may produce clusters that are the progenitors of modern-day halo globular clusters. Future observational work searching for globular clusters around younger galaxies where we expect their typical mass to be less than that found around the Milky Way, and theoretical work exploring more of the high-mass range of the parameter space will be crucial for further demonstrating the connection between halo globular clusters and minihalos.

M. L. A. R. was supported by NSF grant AST11-03608 and the National Science and Engineering Research Council of Canada. E. S. was also supported by the National Science Foundation under grant AST11-03608 and NASA theory grant NNX09AD106. The authors would like to acknowledge the Advanced Computing Center at Arizona State University (URL: <http://a2c2.asu.edu/>), the Pittsburgh Supercomputer Center (PSC) (URL: <http://www.psc.edu/>) and the Texas Advanced Computing Center (TACC) at The University of Texas at Austin (URL: <http://www.tacc.utexas.edu>) for providing HPC resources that have contributed to the research results reported within this paper. The authors would like to thank the Extreme Science and Engineering Discovery Environment for allocation time on TACC and PSC resources. We would like to thank Robert Thacker and Paul Ricker for discussions that greatly improved this study. This work performed under the auspices of the U.S. Department of Energy by Lawrence Livermore National Laboratory under Contract DE-AC52-07NA27344

REFERENCES

- Abel, T., Bryan, G. L., & Norman, M. L. 2002, *Science*, 295, 93
Ahn, K., Shapiro, P. R., Iliev, I. T., Mellema, G., & Pen, U. 2009, *ApJ*, 695, 1430
Armandroff, T. C. 1989, *AJ*, 97, 375
Ashman, K. M., & Bird, C. M. 1993, *AJ*, 106, 2281
Barkana, R., & Loeb, A. 2001, *Phys. Rep.*, 349, 125
Birdsall, C. K., & Fuss, D. 1997, *Journal of Comp. Phys.*, 135, 141
Bower, R. G., Benson, A. J., Malbon, R., et al. 2006, *MNRAS*, 370, 645
Bromm, V., & Clarke, C. J. 2002, *ApJ*, 566, L1
Bruzual, G., & Charlot, S. 2003, *MNRAS*, 344, 1000
Chung, A., Yun, M. S., Narayana, G., Heyer, M., & Erickson, N. R. 2011, *ApJ*, 732, L15
Colella, P., & Glaz, H. M. 1985, *J. Comput. Phys.*, 59, 264
Colella, P., & Woodward, P. 1984, *J. Comput. Phys.*, 54, 174
Cole, S., Lacey, C. G., Baugh, C. M., & Frenk, C. S. 2000, *MNRAS*, 319, 168
Conroy, C., Loeb, A., & Spergel, D. 2011, 741, 72
Davis, M., Efstathiou, G., Frenk, C. S., & White, S. D. M. 1985, *ApJ*, 292, 371
Eisenstein, D. J., & Hut, P. 1998, *ApJ*, 498, 137
Ferrara, A. & Loeb, W. 2013, *MNRAS*, 431, 2826
Franx, M., Illingworth, G. D., Kelson, D. D., van Dokkum, P. G., & Tran, K.W. 1997, *ApJ*, 486, L75
Fryxell, B., Müller, E., & Arnett, B. 1989, *nuas.conf*, 100
Fryxell, B., Olson, K., Ricker, P., et al. 2000, *ApJS*, 131, 273
Fujita, A., Martin, C. L., Mac Low, M.-M., & Abel, T. 2003, *ApJ*, 599, 50
Galli, D., & Palla, F. 1998, *A&A*, 335, 403
Gray, W. J., & Scannapieco, E. 2010, *ApJ*, 718, 417
Gray, W. J., & Scannapieco, E. 2011, *ApJ*, 733, 88
Gray, W. J., & Scannapieco, E. 2011, *ApJ*, 742, 100
Hammer, F., Kaper, L., & Dalton, G. 2010, *The Messenger*, 140, 36
Harris, W. E., Whitmore, B. C., Karakla, D., et al. 2006, *ApJ*, 636, 90
Harris, W. E., Kavelaars, J. J., Hanes, D. A., Pritchett, C. J., & Baum, W. A. 2009, *AJ*, 137, 3314
Heckman, T. M., Lehnert, M. D., Strickland, D. K., & Armus, L. 2000, *ApJ*, 129, 493
Ibata, R., Nipoti, C., Sollima, A., et al. 2013, *MNRAS*, 428, 3648
Katz N., Weinberg D. H., & Hernquist L. 1996, *ApJS*, 105, 19
Kauffmann, G., White, S. D. M., & Guiderdoni, B. 1993, *MNRAS*, 264, 201
Larson, D., Dunkley, J., Hinshaw, G., et al. 2011, *ApJS*, 192, 16
Lehnert, M. D., & Heckman, T. M. 1996, *ApJ*, 462, 651
Lewis, A., Challinor, A., & Lasenby, A. 2000, *ApJ*, 538, 473
Martin, C. L. 1999, *ApJ*, 513, 156
McCarthy, P. 2008, Presentation Made to the Astronomical Society of Australia
Mieske, S., Jordán, A., Côté, P., et al. 2006, *ApJ*, 653, 193
Moore, B. 1996, *ApJ*, 461, L13
Navarro, J. F., Frenk, C. S., & White, S. D. M. 1997, *ApJ*, 490, 493
Osterbrock D. E., 1989, *Astrophysics of Gaseous Nebular and Active Galactic Nuclei* (Mill Valley, CA: Univ. Science Books)

- Ostriker, J. P., Spitzer, L., & Chevalier, R. A. 1972, *ApJ*, 176, L51
- Palla, F., & Galli, D. 2000 in *Molecular hydrogen in space*, ed. Combes, F. and Pineau Des Forets, G., 2001, p. 247
- Peng, E. W., Jordán, A., Blakeslee, J. P., et al. 2009, *ApJ*, 703, 42
- Pettini, M., Kellogg, M., Steidel, C. C., et al. 1998, *ApJ*, 508, 539
- Richardson, M. L. A., Scannapieco, E., & Thacker, R. J. 2013, *ApJ*, 771, 81
- Rupke, D. S., Veilleux, S., & Sanders, D. B. 2005, *ApJS*, 160, 115
- Scannapieco, E., Ferrara, A., & Madau, P. 2002, *ApJ*, 574, 590
- Scannapieco, E., Weisheit, J., & Harlow, F. 2004, *ApJ*, 615, 29
- Spergel, D. N., Bean, R., Dore, O., et al. 2007, *ApJS*, 107, 377
- Spitzer, L., & Thuan, T. X. 1972, *ApJ*, 175, 31
- Springel, V., White, S. D. M., Jenkins, A. et al. 2005, *Natur*, 435, 2
- Springel, V., Yoshida, N., & White, S. D. M. 2001, *Nature*, 6, 79
- Springel, V. 2005, *MNRAS*, 364, 1105
- Stacy, A., Greif, T. H., & Bromm, V. 2010, *MNRAS*, 403, 45
- Steigman G. 2009, in Van Steenberg M. E., Sonneborn G., Moos H. W., Blair W. P., eds, *AIP Conf. Proc. Vol. 1135, Future Directions in Ultraviolet Spectroscopy*. Am. Inst. Phys., Melville, NY, p. 94
- Stiavelli, M., et al. 2008, *JWST Primer*, Version 2.0 (Baltimore, MD: STScI)
- Strader, J., Brodie, J. P., Spitler, L., & Beasley, M. A. 2006, *AJ*, 132, 2333
- Thacker, R. J., & Couchman, H. M. P. 2000, *ApJ*, 545, 728
- Thacker, R. J., Scannapieco, E., & Davis, M. 2002, *ApJ*, 581, 836
- Truelove, J. K., Klein, R. I., McKee, C. F., et al. 1997, *ApJL*, 489, 179
- Turk, M. J., Abel, T., & OShea, B. 2009, *Science*, 325, 601
- Turk, M. J., Smith, B. D., Oishi, J. S., et al. 2011, *ApJS*, 192, 9
- Veilleux, S., Cecil, G., & Bland-Hawthorn, J. 2005, *ARA&A*, 43, 769
- Whalen, D., OShea, B. W., Smidt, J., & Norman, M. L. 2008, *ApJ*, 679, 925
- White, S. D. M., & Frenk, C. S. 1991, *ApJ*, 379, 52
- White, S. D. M., & Rees, M. J. 1978, *MNRAS*, 183, 341
- Wright, S., & Barton, B. 2009, *IRIS Sensitivities, Simulations and Astrometry Update*, TMT.INS.PRE.09.037
- Zinn, R. 1985, *ApJ*, 293, 424